

Street canyon ventilation and airborne pollution dispersion: 2-D versus 3-D CFD simulations

Article

Accepted Version

Creative Commons: Attribution-Noncommercial-No Derivative Works 4.0

Mei, S.-J., Luo, Z. ORCID: <https://orcid.org/0000-0002-2082-3958>, Zhao, F.-Y. and Wang, H.-Q. (2019) Street canyon ventilation and airborne pollution dispersion: 2-D versus 3-D CFD simulations. *Sustainable Cities and Society*, 50. 101700. ISSN 2210-6707 doi: <https://doi.org/10.1016/j.scs.2019.101700> Available at <https://centaur.reading.ac.uk/84719/>

It is advisable to refer to the publisher's version if you intend to cite from the work. See [Guidance on citing](#).

To link to this article DOI: <http://dx.doi.org/10.1016/j.scs.2019.101700>

Publisher: Elsevier

All outputs in CentAUR are protected by Intellectual Property Rights law, including copyright law. Copyright and IPR is retained by the creators or other copyright holders. Terms and conditions for use of this material are defined in the [End User Agreement](#).

www.reading.ac.uk/centaur

CentAUR

Central Archive at the University of Reading

Reading's research outputs online

1 *Manuscript revised for Sustainable Cities and Society, 2019*

2

3 **Street canyon ventilation and air pollution dispersion: 2-D versus 3-D CFD**
4 **simulations**

5

6 Shuo-Jun Mei^{abc}, Zhiwen Luo^{c*}, Fu-Yun Zhao^{ab*} Han-Qing Wang^d

7 (a) School of Power and Mechanical Engineering, Wuhan University, Wuhan, Hubei Province,
8 China

9 (b) Shenzhen Research Institute, Wuhan University, Shenzhen, Guangdong Province, China

10 (c) School of the Built Environment, University of Reading, Reading, United Kingdom

11 (d) School of Civil Engineering, University of South China, Hengyang, Hunan Province, China

12

13 ** Corresponding author:*

14 (1) Dr Zhiwen Luo, School of the Built Environment, University of Reading, United Kingdom;

15 E-mail: z.luo@reading.ac.uk

16 (2) Prof. Fu-Yun Zhao, School of Power and Mechanical Engineering, Wuhan University,

17 Wuhan, Hubei Province, China; E-mail: fyzhao@whu.edu.cn

18

19

20

21

22

23

24

25

26

27

28 **Abstract**

29 Urban ventilation is important for building a healthy urban living environment. 2-D CFD
30 simulation has been used widely for street canyon ventilation due to its computational
31 efficiency, but its applicability for a 3-D simulation has never been studied. This paper
32 tried to answer the question: if and under what conditions, the widely-adopted 2-D CFD
33 simulations on street canyon ventilation can represent real 3-D scenarios? 3-D
34 simulations on street canyons with various street lengths and corresponding 2-D
35 simulations are carried out with RNG $k-\varepsilon$ model. Our study identified two important
36 ventilation mechanism for controlling ventilation and dispersion in a 3-D street canyon,
37 i.e., canyon vortex on the canyon top and the corner vortices at the street ends. The relative
38 importance of these two driving forces will change with the street length/street width ratio
39 (B/W). For isolated street canyon, when B/W is higher than 20 (for $H/W=1$) and 70
40 ($H/W=2$), the street canyon ventilation will be dominated by canyon vortex, and 3-D street
41 canyon ventilation could be simplified as a 2-D case. For multiple street canyon, the
42 threshold of B/W will become 20 when $H/W=1$, and 50 when $H/W=2$. The findings in this
43 study could improve our approaches for simulating urban ventilation.

44 **Keywords**

45 CFD, Corner vortices, Street canyon, Urban ventilation

46 **1. Introduction**

47 A 'street canyon' refers to a narrow space between buildings that line up continuously
48 along both sides of a street (Li et al., 2006). It has a unique climate where micro-scale
49 meteorological processes dominate (Oke, 1988). Pollutants emitted at the ground level
50 considerably deteriorate the local air quality and impose direct impacts on human health.
51 The highest level of pollution and the most outdoor human activities are both concentrated
52 at street canyons, causing the most serious health threat. (Vardoulakis et al., 2003). The

53 thermal comfort of pedestrians is also related to the street canyon geometries
54 (Chatzidimitriou and Yannas, 2013; Syafii et al., 2017). The pedestrian wind environment
55 and thermal comfort could be improved by intentionally designing the street canyon (Du
56 et al., 2019). Understanding the airflow and pollutant dispersion within the urban street
57 canyon is important to the sustainability of the urban environment.

58 The wind flows in the street canyons are inherently complex and exhibit a wide range
59 of physical characteristics including large low-speed areas, strong pressure gradients,
60 unsteady flow regions, three-dimensional effects and wakes (Deck, 2005). These wind
61 flow mechanisms are strongly related to geometry configurations and incoming wind
62 directions. The most widely studied cases in the literature are those with wind
63 perpendicular to the street axis because they represent the worst situation for air pollutant
64 dispersion (Li et al., 2006). Under such wind direction, it is reasonable to assume that the
65 street is infinitely long. Then, the original complex 3-D problem could be simplified as a
66 2-D one.

67 There are two types of 2D cases in previous studies: pure (only 2 directions are
68 simulated) and quasi 2D (all three directions are simulated for a quasi-infinitely long
69 street canyon using lateral periodic boundary conditions). In the 2-D cases, the most
70 important geometrical feature of a street canyon is the aspect ratio, which is the height
71 (H) of the canyon being divided by the width (W). Oke (1988) suggested that the flow
72 within 2-D street canyon could be described in terms of three regimes depending on the

73 aspect ratio (H/W) (Oke, 1988). From a three-dimensional point of view, the length (B),
74 which usually expresses the road distance between two major intersections of the canyon,
75 represents another important geometrical feature of the street canyon. The airflow in the
76 street ends is characterized by horizontal corner vortices. Soulhac et al., (2009) concluded
77 that the flow and dispersion at the street ends were dominated by a large vertical-axis
78 recirculating vortex, which has an important influence on exchanges between the streets
79 and overlying atmosphere. Carpentieri and Robins (2010) measured the mean and
80 turbulent tracer fluxes within several street intersections in a wind tunnel model of a real
81 urban area located in Central London. They found an increase in turbulent exchange at
82 roof level at the intersections (Carpentieri et al., 2012). Their later wind tunnel
83 measurements indicated that complex advective patterns appeared at intersections
84 composed of very simple and regular geometries (Carpentieri et al., 2018). Michioka et
85 al., (2014) conducted a series of large-eddy simulations of 3D street canyons with
86 multiple street lengths. Their simulations show that the mean concentration within the
87 canyon decreased with street length B due to stronger lateral dispersion. The DNS (direct
88 numerical simulation) study of Coceal et al. (2014) showed that the complicated flow
89 pattern had a significant influence on dispersion and mixing within the intersection. Based
90 on the wind tunnel measurements, Nosek et al., (2017) calculated the pollution flux
91 (turbulent and advective) at the lateral openings of three different 3D street canyons when
92 the wind was perpendicular and oblique to the along-canyon axis. Their results confirmed

93 that the buildings' roof-height variability at the intersections plays an important role in
94 the dispersion of the traffic pollutants within 3D canyons.

95 Riain et al. (1998) summarized that the dispersion of gaseous pollutants in a street
96 canyon depended on the air exchange rate at the openings of street canyons, including the
97 roof of the street canyon and street ends. Vardoulakis et al. (2003) subdivided street
98 canyons into short ($B/H \approx 3$), medium ($B/H \approx 5$) and long canyons ($B/H \approx 7$) based on the
99 street length. In relatively short canyons, corner vortices might be strong enough to inhibit
100 the formation of a stable vortex perpendicular to the street in the mid-section. With the
101 increase of street length, this ventilation effect will become less important (Theurer,
102 1999). Chan et al. (2001) found that the B/H ratio can also affect the pollutant
103 concentration inside street canyons. Their later study found that the correlation between
104 pollutant concentration and B/H is due to the vortices generated at the street ends (Chan
105 et al., 2003). Xue and Li (2017) simulated the pollutant dispersion within 3D street
106 canyons and found a maximum pollutant concentration at the symmetry plane and
107 minimum pollutant concentration at street ends. All these important features which are
108 evident in 3-D street canyons are normally neglected in the 2-D airflow and ventilation
109 simulations. In LES studies, although 3-D computation domain is widely used, the streets
110 are usually assumed as infinitely long by using periodic boundary condition at side
111 boundaries to reduce computational cost (Lateb et al., 2016).

112 In the past two decades, there have been many modeling and experimental studies
113 focusing on 2-D canyon cases (Magnusson et al., 2014; Ngan and Lo, 2016; Marciotto
114 and Fisch, 2013; Koutsourakis et al., 2012). Previous studies show significant
115 differences in airflow and dispersion between 3-D and 2-D canyons (Nosek et al., 2017;
116 Xue and Li, 2017). However, it is still not clear when and how well the 2-D models could
117 represent the airflow and pollutant dispersion in the 3D scenarios. As many urban design
118 guidelines were based on previous studies with 2D model, it is necessary to find out the
119 differences between 3D and 2D simulations. Additionally, the 2D simulation can
120 extensively reduce the computational resource, especially at LES scenarios. In the near
121 future, the quasi-2D model is expected to be widely used in LES studies. The present
122 paper attempts to identify requirements that the ventilation at 3-D street canyon can be
123 represented by 2-D models. Specifically, the main research questions are:

124 • Can a 2-D model represent a real 3-D street canyon for street canyon ventilation
125 simulation?

126 • Is there a minimum street length/height ratio that a 2-D model could represent a 3-D
127 street canyon?

128 These questions are explored by conducting a series of 3-D simulations with different
129 street lengths and comparing against a corresponding 2-D simulation. The ambient wind
130 is assumed perpendicular to the street direction at 3-D scenarios. Different indicators such
131 as ACH, normalized concentration, retention time are used as metrics to evaluate the

132 ventilation and air pollution dispersion performance. This paper is structured as follows.
133 The details of the model geometries and methodology are given in Section 2. In Section
134 3, the results are presented by looking at the flow and concentration fields along with
135 multiple ventilation indices. Conclusions are presented in Section 4.

136

137 **2. Methodology**

138 The airflow in the urban area is considered as isothermal and the buoyancy effect is
139 neglected. The time-averaged velocity and concentration fields are predicted using the
140 Reynolds-averaged Navier–Stokes equations (RANS). The open source CFD
141 (computational fluid dynamics) codes OpenFOAM v4.0 is used to solve governing
142 equations of fluid dynamics. The data from wind tunnel experiments carried out by
143 Tominaga and Stathopoulos (2011) is used to validate the computational model.

144 **2.1. Domain dimensions**

145 Figure 1 shows two types of street canyon model adopted here, including the isolated
146 street canyon (ISC) and the multiple street canyon (MSC). Perret et al (2017) evaluated
147 the large-scale unsteadiness of the shear layer separating from an upstream canyon edge
148 on the vertical mass-exchange of the street canyon by wind tunnel measurement. It is
149 suggested that the influence of the upstream buildings could not be simply ignored.
150 Therefore, for the MSC configuration, we consider four canyons upstream and three
151 canyons downstream of the target canyon. As the target canyon is far away from the flow
152 separation at the leading edge, the airflow pattern at downstream canyons keeps
153 unchanged (Mei et al., 2017). The width of the street canyons is fixed at $W = 0.1$ m, while
154 the height of the buildings H varies to form different aspect ratios (H/W), i.e., $H/W=1.0$
155 and 2.0. All the cases considered fall into the skimming flow regime in the canyon (Oke,
156 1988). The building length B varies from $4W$ to $60W$ and the ambient wind blows
157 perpendicular to the street canyon. The computational domain is selected based on the

158 best practice guidelines for CFD simulation of urban aerodynamics (Franke, 2007;
159 Tominaga et al., 2008). The upstream distance and downstream distance are $5H$ and 15
160 H respectively. The domain height is $8H$ and the side distances are $5H$. A passive pollutant
161 is released at a line source at the centre of the street.

162 **2.2. Boundary conditions**

163 The inlet profiles are set based on the wind tunnel measurement of Tominaga and
164 Stathopoulos (2011). The vertical profile of mean velocity in the approaching flow
165 approximately obeys a power law with an exponent of 0.26. The upwind mean velocity
166 U_{ref} at building height $h (= W)$ is 3.8 m/s. A no-slip boundary condition is imposed at the
167 building surfaces and the bottom boundary of the domain. The ground and building
168 surface roughness are ignored in the simulation. The top and lateral boundaries of the
169 domain are set as free-slip. On the outflow boundary, a zero diffusive flux is imposed for
170 all flow variables in the direction normal to the outflow plane. This means that the
171 conditions of the outflow plane are extrapolated from within the domain. This assumption
172 is valid for fully developed flows.

173 **2.3. Computational meshes**

174 Unstructured hexahedral meshes are generated by snappyHexMesh (OpenCFD Ltd,
175 v4.0) using the cutCell assembly meshing function. The domain near the buildings and
176 ground contains the smallest grids, cubic cells with dimensions of $0.05W \times 0.05W \times$
177 $0.05W$. To reduce the computational load, sparser grids are used in the regions away from
178 the buildings and ground. The largest cubic cells are with dimensions of $0.2W \times 0.2W \times$
179 $0.2W$. The total number of grids ranges from 0.6 to 7.8 million, depending on buildings'
180 length B and canyon number.

181 The grid-independency test was conducted by comparing three types of mesh (coarse,
182 basic and refined mesh) for the single canyon case with $B/W = 4$. The coarse and refined
183 meshes were built by reducing and increasing the mesh number between buildings by 1.5
184 times, respectively. The mean velocity and turbulent kinetic energy (TKE) at the middle

185 line (along y -direction) at the roof of street canyon calculated between three meshes are
 186 compared in Fig. 2. By further increasing the mesh number (from basic to refined mesh),
 187 both velocity and turbulent kinetic energy (TKE) fields showed little changes, which
 188 shows that the present grid is sufficiently dense for the present studies.

189

190 **2.4. Solution method**

191 The atmospheric air can then be assumed incompressible. In 2-D RANS modeling, the
 192 flow properties are disintegrated into their mean and fluctuating components by Reynolds
 193 decomposition and substituted in the Navier–Stokes equations, which could be written as:

$$194 \quad \frac{\partial \bar{u}_i}{\partial x_i} = 0 \quad (1)$$

$$195 \quad \frac{\partial \bar{u}_i}{\partial t} + \frac{\partial}{\partial x_j} (\overline{u_i u_j}) = -\frac{\partial \bar{p}}{\partial x_i} + \frac{\partial}{\partial x_i} (\overline{\tau_{ij}} - \overline{u_i u_j}) \quad (2)$$

196 where x_i are the Cartesian coordinates. The mean and fluctuating components of flow
 197 properties are marked with overbar and apostrophe respectively. For example, \bar{u}_i
 198 represents the components of the mean velocity. Here, \bar{p} is the pressure, $\overline{u_i u_j}$ the
 199 Reynolds stress tensor which remains after the hydrostatic pressure is removed. The
 200 Reynolds stress tensor appearing in the mean momentum equation is modeled using the
 201 Boussinesq's eddy viscosity model:

$$202 \quad \overline{u_i u_j} = 2\nu_t \overline{S_{ij}} - \frac{2}{3} k \delta_{ij} \quad (3)$$

203 where the strain rate tensor $\overline{S_{ij}} = \frac{1}{2} \left(\frac{\partial u_i}{\partial x_j} + \frac{\partial u_j}{\partial x_i} \right) - \frac{1}{3} \left(\frac{\partial u_i}{\partial x_i} \right) \delta_{ij}$, k denotes the turbulent

204 kinetic energy and ν_t the turbulent viscosity. The RNG k - ϵ model (Yakhot and Orszag,

205 1986) is selected due to its generally good performance in predicting flow around
206 buildings (Tominaga and Stathopoulos, 2010). The steady transport equation for the time-
207 averaged pollutant concentration (\bar{c} , kg/ m³) is:

$$208 \quad \bar{u}_j \frac{\partial \bar{c}}{\partial x_j} = \frac{\partial}{\partial x_j} (K_c \frac{\partial \bar{c}}{\partial x_j}) + Q \quad (4)$$

209 where \bar{u}_j is the time-averaged velocity components, Q is the pollutant emission rate,
210 $K_c = \nu_t/S_{ct}$ is the turbulent eddy diffusivity of pollutants, ν_t is the kinematic eddy viscosity,
211 $S_{ct} = 0.7$ is the turbulent Schmidt number (Di Sabatino et al., 2007).

212 All transport equations are discretized using a finite volume method. The hybrid second
213 order upwind/central differencing scheme is utilized to discretize the advection terms,
214 with an option of the second-order upwind scheme and the QUICK scheme (Patankar,
215 1980). The discretized differential equations are solved by the SIMPLE algorithm
216 (Patankar, 1980), which is solved by simpleFOAM solver in OpenFOAM .

217 Convergence is achieved when all scaled residuals are less than 10^{-5} and the average
218 flow speeds at several locations.

219

220 **2.5. Model validation**

221 Model validation is essential for CFD studies before further analysing. The accuracy of
222 the current CFD model is demonstrated by comparing to the experimental database
223 obtained from the wind tunnel at Niigata Institute of Technology (Tominaga and
224 Stathopoulos, 2011). The three-dimensional canyon was characterized with $H/W = 1.0$
225 and $H/B = 0.5$. Ethylene (C₂H₄) was used as a tracer gas and released at the centre of the
226 street bottom with a concentration of 1000 ppm. The pollutant was released by a point
227 source in their experiment. The atmospheric boundary flow profiles were produced by a
228 combination of spires and surface roughness in their experiment. The velocity and
229 turbulent profiles could be represented by $U(z) = U_{ref}(z/H)^{0.26}$. $k(z) = (U(z)I(z))^2$,

230 $\varepsilon = \sqrt{C_\mu} k(z) \frac{dU(z)}{dz}$, according to their measurement. The inlet profiles have been
 231 compared to the measurement of Tominaga and Stathopoulos (2011) in Fig. 3. Here,
 232 $U_{\text{ref}} = 3.8$ m/s. $C_\mu = 0.0845$, is a constant in the RNG turbulent model, $I(z)$ is the turbulent
 233 intensity.

234 The velocity vectors on the vertical and horizontal planes were compared with the wind
 235 tunnel experiment in Figs. 4a and 4b. On the vertical section at the middle point, a single
 236 recirculation flow was observed in the street canyons. On a horizontal section at $z/H =$
 237 0.1, two vortices appeared within the street canyons. The general patterns of the
 238 recirculation flow in CFD were close to that in the experiment. Figure 4d, 4e and 4f
 239 compared the measured and calculated concentration \bar{c} along the streamwise direction
 240 (x). Overall, the CFD prediction of \bar{c} is satisfactory. Despite overestimation is found at
 241 the height of $z/H = 0.1$, it is consistent with previous RANS simulations (Gromke et al.,
 242 2008; Tominaga and Stathopoulos, 2011). These differences were caused by
 243 underestimated turbulence diffusions in lateral direction in RANS models.

244 In order to evaluate the predictions of a model with experimental observations, the
 245 normalized mean square error (*NMSE*) recommended by Hanna et al. (1991) were used,
 246 which represents the normalized discrepancy between the computed and experimental
 247 values and is calculated as follows,

$$248 \quad NMSE = \frac{\sum_{i=1}^n (O_i - P_i)^2}{\sum_{i=1}^n (O_i P_i)} \quad (5)$$

249 where n represents the number of points, O_i represents the measurements at each point
 250 and \bar{O} is the measurement mean. P_i and \bar{P} represent the computed values and the
 251 corresponding mean at each point, respectively. A perfect model could have the
 252 parametric values of $NMSE = 0.0$. According to the recommended criteria by COST

253 Action 732 (Efthimiou et al., 2011), ‘state of the art’ model performance has met the
254 following statistical metrics standard: $NMSE < 1.5$. The calculated $NMSE$ at the bottom
255 line, middle line and top line are 0.128, 0.182 and 0.412, respectively. As the focus of the
256 present study is on evaluating the difference in pollutant dispersion between two-
257 dimensional and three-dimensional RNAS models, the numerical model used in this study
258 is considered reliable.

259

260 **3. Results and discussion**

261 **3.1. Three-dimensional street canyon airflow**

262 Dispersion within three-dimensional street canyon is heavily influenced by the flow
263 structure. Therefore, we begin by describing the basic flow pattern within a street canyon
264 surrounded by urban buildings and subjected to perpendicular approaching wind, as
265 shown in Fig. 5. Gromke and Ruck (2007) summarized that there are two distinguishable
266 flow characteristics, i.e., vertically rotating (recirculating with the along-canyon axis)
267 canyon vortices and horizontally rotating (recirculating with the vertical axis) corner
268 eddies. The canyon vortices are driven by shear forces of the skimming flow above the
269 rooftop. Instead, the corner vortices are driven by the shear at street ends, which is
270 induced by the channelling flow. The resulting flow in a 3-D street canyon could be more
271 complex due to the interaction between the corner vortices and canyon vortices. Becker
272 et al. (2002) and Kim and Baik (2004) found a portal vortex behind the upwind building,
273 which extends toward the lower edges of the downwind building.

274 The flow structure is depicted by tracing a set of streamlines originated from multiple
275 seed locations on a straight line above the line source ($z/H = 0.1$), shown in Fig. 6. The
276 streamlines are coloured by mean velocity. Here, cases with $B/W = 4$ are selected for
277 illustration. The basic characteristics described by Gromke and Ruck (2007) are also

278 found in streamlines. However, for the ISC configuration, the corner vortices extend
279 beyond the street ends toward the upwind corner. This is because of the reverse flow near
280 the side walls induced by the flow separation (Murakami and Mochida, 1989). In contrast,
281 the corner vortices are well confined within the canyon volume in the MSC configuration.
282 This is because the target canyon is far away from the leading building and not influenced
283 by the flow separation. The $y/B = 0$ planes represent the symmetrical planes and $y/B =$
284 ± 0.5 represent the street ends.

285 The x -velocity was filtered as zero to transfer the 3D streamlines to 2D streamlines.
286 The 2D streamlines in the ISC case ($B/W = 4$) were plotted at planes parallel to the street
287 direction to show the flow structure along the street direction. The planes were located at
288 the centrelines of the streets, shown as Fig. 7. A counter-rotating flow structure was
289 observed at the y - z plane. This flow structure induced ambient air from the street ends
290 into the street canyon volume. The inlet flows at two street ends were of opposite
291 directions and collided at the symmetry plane, resulting with an upward flow.

292 It is interesting to note that mean streamlines escapes from the canyon roof at the
293 symmetrical planes, instead of recirculating below roof level. When the streamlines
294 recirculate below the roof level, the pollutant is transported mainly due to turbulence
295 (Buccolieri et al., 2009). However, the mean upward flow extended beyond the roof level
296 could extensively raise the mass transfer rate. Fig. 8 shows contours plots of the
297 normalized vertical velocity w^* ($= w/U_{\text{ref}}$, where w is the mean vertical velocity) at two
298 different height $z = 0.1H$ and $z = 1.0H$. Strong upward flow is observed at both heights.
299 The upward flow is confined within a narrow area adjacent to the upwind buildings except
300 at the symmetrical planes, where the upward flow extends across the whole street canyon
301 width. This indicates that pollutants may be transferred directly from ground level to roof
302 level at symmetrical planes (refers to the x - z plane at $y = 0$). This statement could be
303 supported by abnormal pollutant concentration decay at that position, which is also
304 observed in previous wind tunnel experiment (Gromke, 2011; Gromke and Ruck, 2012)

305 and CFD simulations (Jeanjean et al., 2015). In fact, the concentration drop in the
306 symmetry plane is not common in previous studies. There are several reasons: 1) the point
307 sources instead of line sources were used in previous 3D street canyon studies; 2) the
308 concentration drops were only observed at specific street length range; when street is long
309 enough, the concentration drop is no longer obvious, as shown as Fig. 15. 3) the
310 surrounding buildings (with intersections) are ignored in the present studies, which could
311 potentially suppress the horizontal convergence flow, as shown in Fig. 7

312 **3.2. Pollutant dispersion at the three-dimensional street canyon**

313 To facilitate the comparison among the 2-D and 3-D simulations, dimensionless
314 concentration C is introduced as a function of the simulated pollutant concentration \bar{c}
315 (kg/m^3), reference wind speed U_{ref} (m/s), height of the building H (m), length of the line
316 source B (m), and ethane flow rate Q (kg/s) (Meroney et al., 1996),

317

$$318 \quad C = \frac{\bar{c} U_{\text{ref}} H B}{Q} \quad (6)$$

319 The dimensionless concentration fields at three x - z planes of 3-D street canyons along
320 with the corresponding 2-D cases are shown in Fig. 9 and Fig. 10. Generally, the
321 concentration distributions in these planes of 3-D simulation are different than those in
322 the case of the 2D canyon. The concentration levels are appreciably lower at $y/B = 0$
323 planes, which is due to strong upward flow as described in the former section. The
324 pollutant concentration are even lower at the $y/B = 0.45$ planes, where are close to the
325 street ends. The corner vortices at street ends could significantly enhance the local
326 dilution rate (Buccolieri et al., 2009). An appreciably higher concentration is observed at
327 the street level at $y/B = 0.25$ planes, which is quite different from 2-D canyon. This
328 indicates the convergence flow along the street direction has non-negligible influence on
329 the pollutant dispersion. These differences remain at the very long street ($B/W = 60$). It

330 should be cautious when applying 2-D model to predict the pollutant distribution in street
 331 canyon

332

333 **3.3 Ventilation in the street canyon**

334 The pollutant dilution at the 2-D street canyon is governed by the air exchange at roof
 335 level, while for the 3-D street canyon, ventilation both at the roof level and street ends
 336 will play its role. The averaged ACH_{roof} (Hang and Li, 2010) is used to evaluate the air
 337 exchange at the street canyon roof, which is divided into the mean component:

$$338 \quad \overline{ACH}_{roof} = \frac{1}{HBW} \int_{\Gamma_{roof}} \overline{w}_+ dx dy, \quad (7)$$

339 and the turbulent component:

$$340 \quad ACH'_{roof} = \frac{1}{HBW} \int_{\Gamma_{roof}} \frac{1}{2} \sqrt{w'w'} dx = \frac{1}{HBW} \int_{\Gamma_{roof}} \sqrt{\left[\frac{k}{6} - \frac{1}{2} v_t \left(\frac{\partial \overline{w}}{\partial z} \right) \right]} dx dy, \quad (8)$$

341 where w is the vertical velocity component, v_t the turbulent viscosity and Γ_{roof} the roof
 342 area of the street canyon. The subscript + signifies that only the upward velocity $w > 0$
 343 (i.e., air removal) is considered.

344 Similarly, the ACH_{side} at street ends is calculated as:

$$345 \quad \overline{ACH}_{side} = \frac{1}{BHW} \int_{\Gamma_{side}} \overline{v}_+ dx dz \quad (9)$$

$$346 \quad ACH'_{side} = \frac{1}{BHW} \int_{\Gamma_{side}} \frac{1}{2} \sqrt{v'v'} dx = \frac{1}{BHW} \int_{\Gamma_{side}} \sqrt{\left[\frac{k}{6} - \frac{1}{2} v_t \left(\frac{\partial \overline{v}}{\partial y} \right) \right]} dx dz \quad (10)$$

347 where v is the velocity ay y-direction component and Γ_{side} the street ends area of the street
 348 canyon. The subscript + signifies that only the outward velocity $v > 0$ (i.e., air removal)
 349 is considered. It should be noted that the v_+ for one street end and v_- for the opposite street
 350 end. The total ventilation for street canyon ACH_c will be the sum of ACH_{roof} and ACH_{side}

$$351 \quad ACH_c = ACH_{roof} + ACH_{side} \quad (11)$$

352 The air exchange rate and its mean and turbulent components at canopy roof as a
353 function of the street length are presented at Fig. 11. The ACH at 2-D simulations is
354 plotted as blue lines. It is found that the ACH_{roof} contributed by mean flow is smaller than
355 turbulent fluctuation for all cases. In the MSC configuration, the mean flows in that
356 configuration are parallel to the roof surfaces, resulting with weak mean vertical flow.
357 Therefore, the turbulent fluctuation (ACH'_{roof}) dominates the air exchange at roof level.
358 Compared to the MSC configuration, the mean flow in the ISC configuration plays a more
359 significant role in the air exchange due to flow separation. It was found that ACH_{roof} were
360 almost unchanged with the increase of street length when streets were long enough.
361 However, the variation trend varies from case to case. For isolated canyon with $H/W =$
362 1.0, the ACH_{roof} increases significantly with the street length. When we increase the H/W
363 to 2.0 at isolated canyon cases, the ACH_{roof} decreases firstly before increases
364 monotonically. This could be due to the flow separation at street ends, which may
365 decrease the shear at roof level.

366 The air exchange rate and its mean and turbulent components at street ends as a function
367 of the street length are presented at Fig. 12. In contrast to street canyon roof, the ACH_{side}
368 has a negative relation with the street length. This explained why there is a peak value for
369 the ACH_c . The functions between the ACH_c and street length are plotted in Fig. 13. When
370 initially increasing the street length, the decrease of ACH at street ends plays a dominant
371 role. As a result, the total ACH increases with the street length. When further increasing
372 the street length, the increase of the ACH at street roof plays a dominant role. Therefore,
373 the total ACH decreases with the street length when B/W is longer than 30.

374 As shown in the flow field at Fig. 6 and Fig. 7, the street length has two opposite effects
375 on the pollutant dispersion. Firstly, with the increase of the street length, the corner
376 vortices have less impact on the pollutant dilution of the whole canyon volume. As a
377 result, the pollutant concentration increased with street length. Secondly, the interaction
378 between the corner vortices and canyon vortices would also be weakened when increasing

379 the street length. As a result, the pollutant concentration would decrease with street
380 length. With continue increasing the street length, the first effect dominants the pollutant
381 dilution and the second one gradually disappears.

382

383 **3.4. Retention time at street canyon**

384 The ventilation performance of the whole canyon will be evaluated by the canyon
385 retention time τ_c (Cheng et al., 2008), calculated as:

$$386 \quad \Theta = \frac{1}{V} \iiint c dx dy dz \quad (12)$$

$$387 \quad \tau_c = \frac{\Theta \times V}{Q} \quad (13)$$

388 where c is the local concentration of a passive tracer gas (kg/m^3), and Q is the pollutant
389 emission rate (kg/s), V the volume of the street canyon. The average pollutant
390 concentration Θ signifies the overall air quality of the street canyon while τ_c represents
391 the time scale for a parcel of pollutant being removed from the street canyon.

392 Figure 14 shows the canyon retention time as a function of the street length. The canyon
393 retention time of 2-D simulation is plotted as blue dash lines. The most important goal
394 for the present study is to find the minimum street length that 2-D simulation can represent
395 the ventilation of 3-D street canyon. In ISC configuration, the minimum street lengths are
396 20W and 70W for $H/W = 1.0$ and 2.0 respectively. In MSC configuration, the minimum
397 street lengths are 20W and 50W for $H/W = 1.0$ and 2.0 respectively.

398 The canyon retention time increases firstly and then decreases to a constant value with
399 the increasing street length. Additionally, the peak value increases with the aspect ratio
400 (H/W). In the ISC configuration, the canyon retention time reaches its maximum value at
401 $B/W = 6$ for $H/W = 1.0$ and at $B/W = 20$ for $H/W = 1.0$. In the MSC configuration, the
402 maximum value of retention time corresponds to $B/W = 8$ and 20 for $H/W = 1.0$ and 2.0,
403 respectively. This is just opposite to variation of the total ACH , which indicates that the
404 air exchange at street openings dominates the pollutant dilution at these cases.

405 In order to show the integrated characteristics of the canopy layer, we average the above
406 quantities inside the street canyon, i.e.

$$407 \quad \Omega_{canyon} = \{(x, z): -0.5W \leq x \leq 0.5W, -0.5B \leq y \leq 0.5B, 0 \leq z \leq H\}:$$

$$408 \quad \bar{\varphi} = \frac{B}{QWH} \int_{-0.5W}^{0.5W} \int_0^H c(x, z) dx dz \quad (14)$$

409 In other words, $\bar{\varphi}$ denotes an average retention time along the y-direction.

410 Figure 15 shows the distribution of retention time along the street direction (y-
411 direction). For the ISC configuration with $H/W = 1.0$, the retention time decreases
412 significantly at the street end, indicating the corner vortices enhanced local dilution rate.
413 Toward the symmetrical planes, the retention time rises rapidly before significant
414 declining in a narrow zone at the symmetrical planes. As explained before, pollutants
415 could be transferred directly from ground level to roof level at symmetrical planes. With
416 the increase of street length, the rise of retention time disappears at symmetrical planes.
417 This indicates that the increase in retention time is caused by interaction between canyon
418 vortex and corner vortices.

419 For the ISC configuration with $H/W = 2.0$, a significant increase of local retention time
420 is found at the street ends. It could be caused by the of corner vortices, which can become
421 more strength at the deep street canyon. However, the increase of retention time at street
422 ends is not found in multiple canyon cases. This suggests that the corner vortices are not
423 driven by shear force at street ends as suggested by Gromke and Ruck (2007). Instead,
424 they are resulted from flow separation at side walls. Such difference could be due to the
425 fact that the skimming flow regime is chosen in the present study.

426 **3.5 Limitations**

427 Although the present RANS model provides satisfactory accuracy, the unsteadiness of
428 the turbulence could not be reproduced. Studies with LES or DNS model are still
429 expected, which could provide more information about the turbulent fluctuation.
430 Moreover, in some previous studies (e.g., Soulhac et al. (2009), Michioka et al. (2014)),

431 that the spatially averaged concentration is the highest at this central plane. In other
432 studies, abnormal concentration decay was found at the central plane (Gromke, 2011;
433 Gromke, and Ruck, 2012). Although we have made some new insight on this issue, there
434 is also a clear need for a set of wind tunnel experimental studies in the future to support
435 our observations. It should also be noted that isolated street canyons instead of street
436 canyons embodied in an urban street network were analysed here. The local flow
437 characteristics could also be affected by surrounding buildings especially intersections.

438

439 **4. Conclusions**

440 In this study, the differences between 2-D and 3-D RANS simulations on resolving the
441 ventilation at street canyon are investigated. The focus is on identifying the threshold
442 value of street length (B) that 2-D results can well represent real 3-D street canyon. Here
443 the skimming flow regime is considered with two aspect ratios ($H/W = 1.0$ and 2.0) for
444 their wide adoption in previous studies. Both isolated street canyon (ISC) and multiple
445 street canyon (MSC) configurations are considered. The air exchange rate and pollutant
446 retention time are used to evaluate the ventilation and pollution dispersion inside the street
447 canyon.

448 With the increase of street length, the differences in ventilation between 3-D and 2-D
449 simulation become insignificant, although there still exists a minor difference between
450 them. A narrow zone with strong upward flow is found at the symmetrical planes at the
451 leeward wall of the street canyon, where an enhanced ventilation is observed. The
452 interaction between this upward flow and vertically rotating vortices at street ends leads
453 to the distinctions between the 3-D and 2-D simulations.

454 With the increase of street length, the averaged retention time of 3-D simulation
455 approaches 2-D simulation. The differences in retention time between 2-D and 3-D
456 simulations disappear when B/W is larger than 20 for $H/W = 1.0$ and 70 for $H/W = 2.0$. In

457 the MSC configuration, the differences disappear when B/W is larger than 20 for $H/W =$
458 1.0 and 50 for $H/W = 2.0$.

459 The correlation between the street length and ventilation capacity could be used in
460 optimizing the urban street design to achieve better air quality. For example, the street
461 length with maximum pollutant accumulation should be avoided in urban design.
462 Additionally, this study could be used in locating the monitoring point for air quality
463 measurement in the street canyons. Monitoring facilities installed in street ends will
464 underestimate the air pollution and overestimate the air pollution at central points.

465

466 **Acknowledgments**

467 The first author wishes to acknowledge the financial support from Wuhan University.
468 Prof. Fu-Yun Zhao would also like to acknowledge the financial support from the Natural
469 Science Foundation of China (NSFC Grant No. 51778504), Fundamental Research
470 Projects from Shenzhen Government (Grant No. JCYJ20160523160857948), and
471 National Key Research and Development Program of the Ministry of Science and
472 Technology of China (Grant No. 2018YFC0705201, Grant No. 2018YFB0904200).

473

474 **References**

- 475 Becker, S., Lienhart, H., Durst, F., 2002. Flow around three-dimensional obstacles in
476 boundary layers. *Journal of Wind Engineering and Industrial Aerodynamics* 90, 265-
477 279.
- 478 Buccolieri, R., Gromke, C., Di Sabatino, S., Ruck, B., 2009. Aerodynamic effects of trees
479 on pollutant concentration in street canyons. *Science of The Total Environment* 407,
480 5247-5256.
- 481 Carpentieri, M., Robins, AG., 2010. Tracer flux balance at an urban canyon intersection.
482 *Boundary-layer meteorology* 135(2), 229-242.

483 Carpentieri, M., Hayden, P., Robins, A.G., 2012. Wind tunnel measurements of pollutant
484 turbulent fluxes in urban intersections. *Atmospheric Environment* 46, 669-674.

485 Carpentieri, M., Robins, A.G., Hayden, P., Santi, E., 2018. Mean and turbulent mass flux
486 measurements in an idealised street network. *Environmental pollution* 234, 356-367.

487 Chan, A.T., Au, W.T.W., So, E.S.P., 2003. Strategic guidelines for street canyon
488 geometry to achieve sustainable street air quality—part II: multiple canopies and
489 canyons. *Atmospheric Environment* 37, 2761-2772.

490 Chan, A.T., So, E.S., Samad, S.C., 2001. Strategic guidelines for street canyon geometry
491 to achieve sustainable street air quality. *Atmospheric Environment* 35, 4089-4098.

492 Chatzidimitriou, A., Yannas, S., 2017. Street canyon design and improvement potential
493 for urban open spaces; the influence of canyon aspect ratio and orientation on
494 microclimate and outdoor comfort. *Sustainable cities and society* 33, 85-101.

495 Cheng, W.C., Liu, C.H., Leung, D.Y.C., 2008. Computational formulation for the
496 evaluation of street canyon ventilation and pollutant removal performance.
497 *Atmospheric Environment* 42, 9041-9051.

498 Coceal, O., Goulart, E.V., Branford, S., Glyn Thomas, T., Belcher, S.E., 2014. Flow
499 structure and near-field dispersion in arrays of building-like obstacles. *Journal of*
500 *Wind Engineering and Industrial Aerodynamics* 125, 52-68.

501 Deck, S., 2005. Zonal-Detached-Eddy Simulation of the Flow Around a High-Lift
502 Configuration. *AIAA Journal* 43, 2372-2384.

503 Di Sabatino, S., Buccolieri, R., Pulvirenti, B., Britter, R., 2007. Simulations of pollutant
504 dispersion within idealised urban-type geometries with CFD and integral models.
505 *Atmospheric Environment* 41(37), 8316-8329.

506 Du, Y., Mak, C.M., Li, Y., 2019. A multi-stage optimization of pedestrian level wind
507 environment and thermal comfort with lift-up design in ideal urban canyons.
508 *Sustainable Cities and Society* 101424.

509 Efthimiou, G., Santiago, J., Martilli, A., 2011. COST 732 in Practice: the MUST
510 ModelEvaluation Exercise.

511 Franke, J., et al., 2007. The COST 732 Best Practice Guideline for CFD simulation of
512 flows in the urban environment: a summary. *International Journal of Environment
513 and Pollution* 44.1.

514 Gromke, C., Buccolieri, R., Di Sabatino, S., Ruck, B., 2008. Dispersion study in a street
515 canyon with tree planting by means of wind tunnel and numerical investigations –
516 Evaluation of CFD data with experimental data. *Atmospheric Environment* 42,
517 8640-8650.

518 Gromke, C., Ruck, B., 2007. Influence of trees on the dispersion of pollutants in an urban
519 street canyon—Experimental investigation of the flow and concentration field.
520 *Atmospheric Environment* 41, 3287-3302.

521 Gromke, C., 2011. A vegetation modeling concept for building and environmental
522 aerodynamics wind tunnel tests and its application in pollutant dispersion studies.
523 *Environmental Pollution* 159(8-9), 2094-2099.

524 Gromke, C., Ruck, B., 2012. Pollutant concentrations in street canyons of different aspect
525 ratio with avenues of trees for various wind directions. *Boundary-Layer
526 Meteorology*, 144(1), 41-64.

527 Hanna, S.R., Strimaitis, D.G., Chang, J.C., 1991. Hazard Response Modelling
528 Uncertainty (A Quantitative Method) Volume II. Evaluation of Commonly-used
529 Hazardous Gas Dispersion Model, Report F08635-89-C-0136, Sigma Research
530 Corporation, Air Force Engineering andService Center, Tyndal Air Force Base
531 Florida, pp. 338.

532 Hang, J., Li, Y., 2010. Wind conditions in idealized building clusters: macroscopic
533 simulations using a porous turbulence model. *Boundary-layer meteorology* 136,
534 129-159.

535 Jeanjean, A. P., Hinchliffe, G., McMullan, W. A., Monks, P. S., Leigh, R.J., 2015. A CFD
536 study on the effectiveness of trees to disperse road traffic emissions at a city scale.
537 Atmospheric Environment 120, 1-14.

538 Kim, J.-J., Baik, J.-J., 2004. A numerical study of the effects of ambient wind direction
539 on flow and dispersion in urban street canyons using the RNG $k-\varepsilon$ turbulence model.
540 Atmospheric Environment 38, 3039-3048.

541 Koutsourakis, N., Bartzis, J.G., Markatos, N.C., 2012. Evaluation of Reynolds stress, $k-$
542 ε and RNG $k-\varepsilon$ turbulence models in street canyon flows using various
543 experimental datasets. Environmental Fluid Mechanics 12, 379-403.

544 Lateb, M., Meroney, R.N., Yataghene, M., Fellouah, H., Saleh, F., Boufadel, M.C., 2016.
545 On the use of numerical modelling for near-field pollutant dispersion in urban
546 environments – A review. Environmental Pollution 208, 271-283.

547 Li, X.-X., Liu, C.-H., Leung, D.Y., Lam, K., 2006. Recent progress in CFD modelling of
548 wind field and pollutant transport in street canyons. Atmospheric Environment 40,
549 5640-5658.

550 Magnusson, S., Dallman, A., Entekhabi, D., Britter, R., Fernando, H.J.S., Norford, L.,
551 2014. On thermally forced flows in urban street canyons. Environmental Fluid
552 Mechanics 14, 1427-1441.

553 Marciotto, E.R., Fisch, G., 2013. Wind tunnel study of turbulent flow past an urban
554 canyon model. Environmental Fluid Mechanics 13, 403-416.

555 Mei, S.-J., Hu, J.-T., Liu, D., Zhao, F.-Y., Li, Y., Wang, Y., Wang, H.-Q., 2017. Wind
556 driven natural ventilation in the idealized building block arrays with multiple urban
557 morphologies and unique package building density. Energy and Buildings 155, 324-
558 338.

559 Meroney, R.N., Pavageau, M., Rafailidis, S., Schatzmann, M., 1996. Study of line source
560 characteristics for 2-D physical modelling of pollutant dispersion in street canyons.
561 Journal of Wind Engineering and Industrial Aerodynamics 62, 37-56.

562 Michioka, T., Takimoto, H., Sato, A., 2014. Large-eddy simulation of pollutant removal
563 from a three-dimensional street canyon. *Boundary-layer meteorology* 150(2), 259-
564 275.

565 Murakami, S., Mochida, A., 1989. Three-dimensional numerical simulation of turbulent
566 flow around buildings using the $k-\varepsilon$ turbulence model. *Building and Environment*
567 24, 51-64.

568 Ngan, K., Lo, K.W., 2016. Revisiting the flow regimes for urban street canyons using the
569 numerical Green's function. *Environmental Fluid Mechanics* 16, 313-334.

570 Nosek, Š., Kukačka, L., Jurčáková, K., Kellnerová, R., Jaňour, Z., 2017. Impact of roof
571 height non-uniformity on pollutant transport between a street canyon and
572 intersections. *Environmental Pollution* 227, 125-138.

573 Oke, T.R., 1988. Street design and urban canopy layer climate. *Energy and buildings* 11,
574 103-113.

575 Patankar, S., 1980. *Numerical heat transfer and fluid flow*. CRC Press.

576 Perret, L., Blackman, K., Fernandes, R., Savory, E., 2017. Relating street canyon vertical
577 mass-exchange to upstream flow regime and canyon geometry. *Sustainable cities*
578 *and society* 30, 49-57.

579 Riain, C.M., Fisher, B., Martin, C.J., Littler, J., 1998. Flow Field and Pollution Dispersion
580 in a Central London Street. *Environmental Monitoring and Assessment* 52, 299-314.

581 Soulhac L, Garbero V, Salizzoni P, et al. Flow and dispersion in street intersections [J].
582 *Atmospheric Environment*, 2009, 43(18): 2981-2996.

583

584 Syafii, NI., Ichinose, M., Kumakura, E., Jusuf, SK., Chigusaa, K., Wong, NH., 2017.
585 Thermal environment assessment around bodies of water in urban canyons: A scale
586 model study. *Sustainable cities and society* 34, 79-89.

587 Theurer, W., 1999. Typical building arrangements for urban air pollution modelling.
588 *Atmospheric Environment* 33, 4057-4066.

589 Tominaga, Y., Mochida, A., Yoshie, R., Kataoka, H., Nozu, T., Yoshikawa, M.,
590 Shirasawa, T., 2008. AIJ guidelines for practical applications of CFD to pedestrian
591 wind environment around buildings. *Journal of Wind Engineering and Industrial*
592 *Aerodynamics* 96, 1749-1761.

593 Tominaga, Y., Stathopoulos, T., 2010. Numerical simulation of dispersion around an
594 isolated cubic building: Model evaluation of RANS and LES. *Building and*
595 *Environment* 45, 2231-2239.

596 Tominaga, Y., Stathopoulos, T., 2011. CFD modeling of pollution dispersion in a street
597 canyon: Comparison between LES and RANS. *Journal of Wind Engineering and*
598 *Industrial Aerodynamics* 99, 340-348.

599 Vardoulakis, S., Fisher, B.E., Pericleous, K., Gonzalez-Flesca, N., 2003. Modelling air
600 quality in street canyons: a review. *Atmospheric environment* 37, 155-182.

601 Xue, F., Li, X., 2017. The impact of roadside trees on traffic released PM10 in urban
602 street canyon: Aerodynamic and deposition effects. *Sustainable cities and society*
603 30, 195-204.

604 Yakhot, V., Orszag, S.A., 1986. Renormalization-group analysis of turbulence. *Physical*
605 *review letters* 57, 1722.

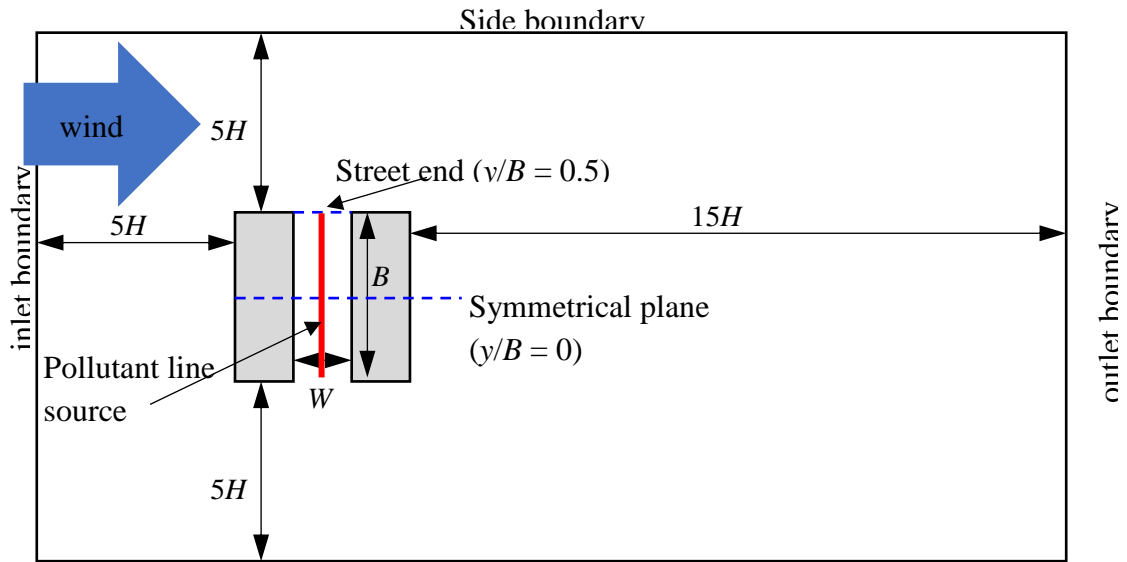
606

607 **Figures and tables**

608 Figure 1

609

610



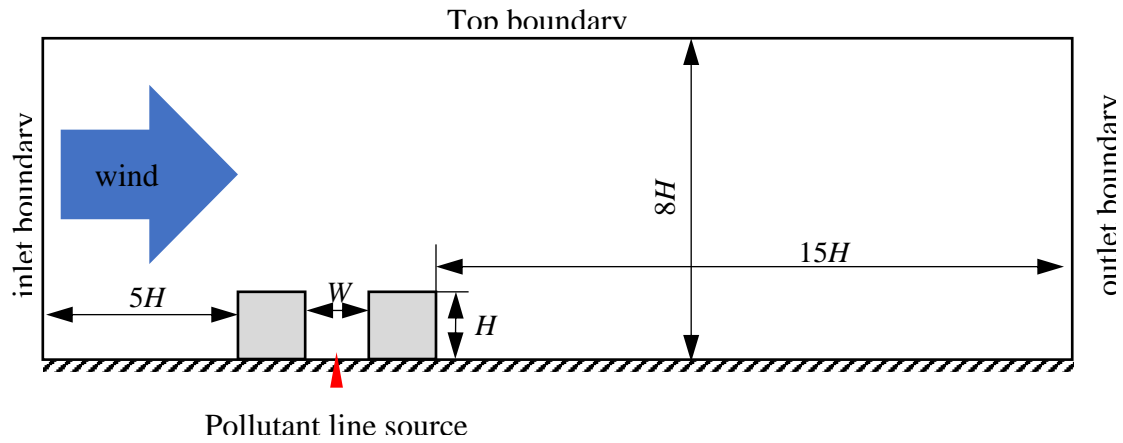
611

Side boundary

612

(a)

613



614

615

616

617

618

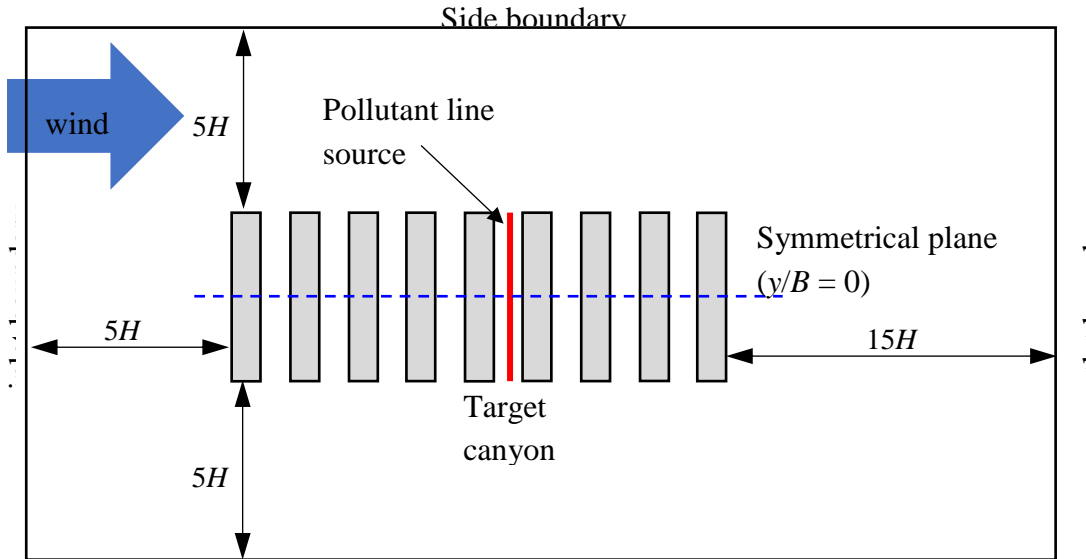
619

620

621

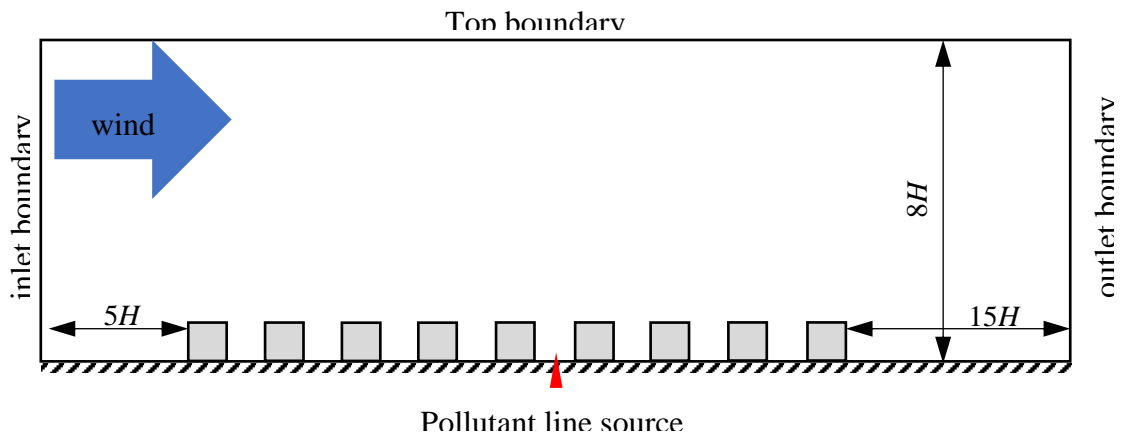
(b)

622
623
624



625
626

Side boundary
(c)



627
628
629
630
631
632
633
634
635
636
637

Fig. 1. Schematic view of computational domains used in CFD studies: (a) top view for isolated canyon and (b) side view for isolated canyon configuration, (c) top view for multiple canyons and (d) side view for multiple canyons configuration.

638 Figure 2

639

640

641

642

643

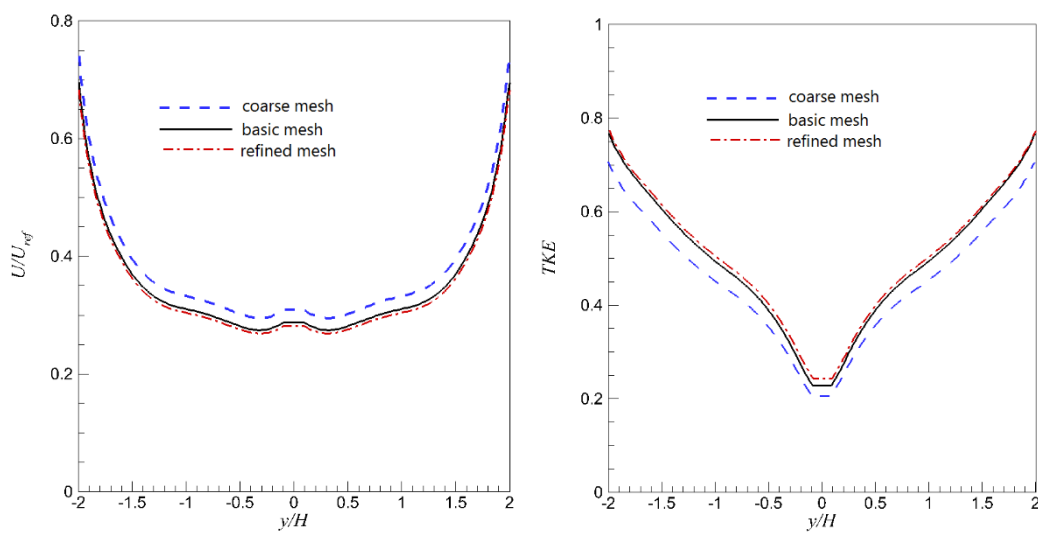
644

645

646

647

648



649

650

651 Fig. 3. Comparison of mean velocity (a) and turbulent kinetic energy (TKE) (b) at middle
652 line (along y-direction) at the roof of single canyon case with $B/W = 4$.

653

654 Figure 3

655

656

657

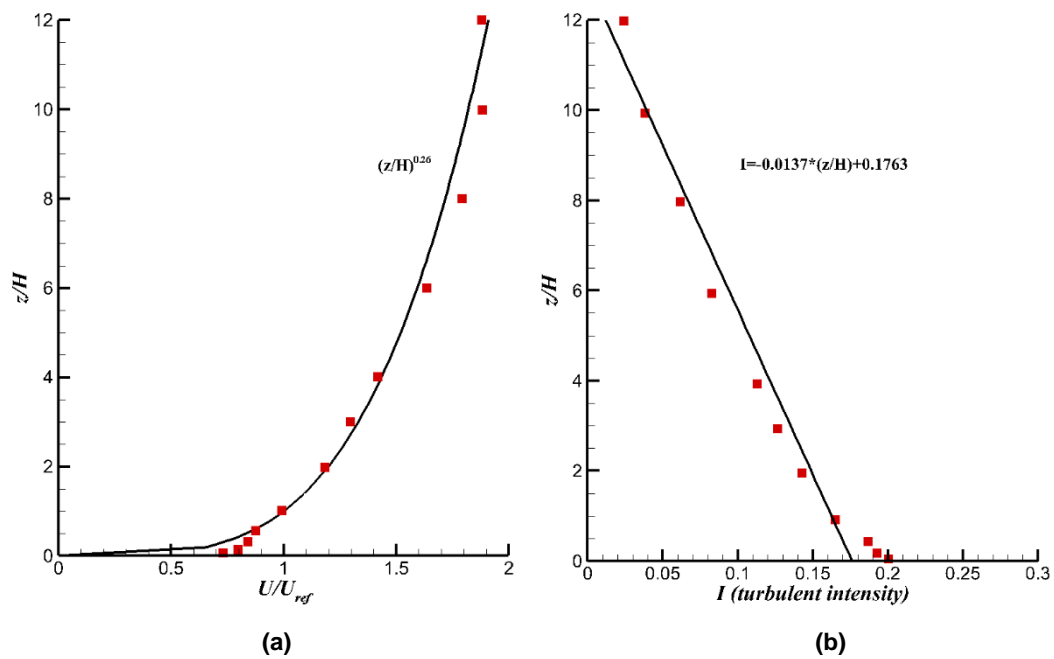
658

659

660

661

662



663

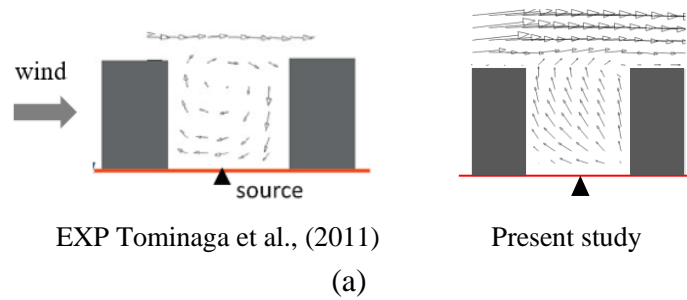
664 **Fig. 3.** Comparisons of CFD inlet velocity (a) and turbulent intensity (b) profiles with
665 measurements from Tominaga and Stathopoulos (2011).

666

667 Figure 4

668

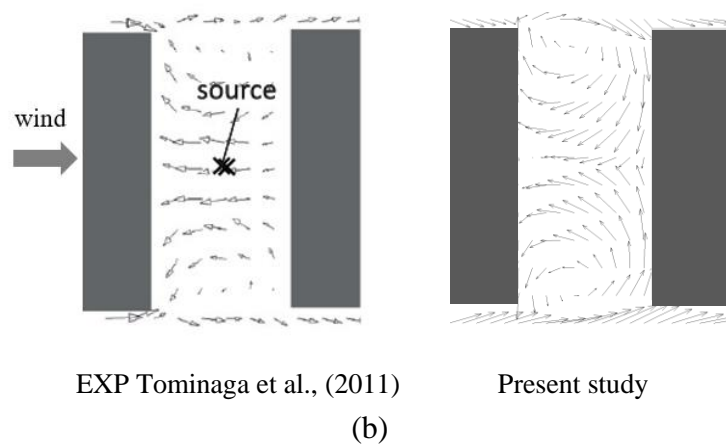
669



674

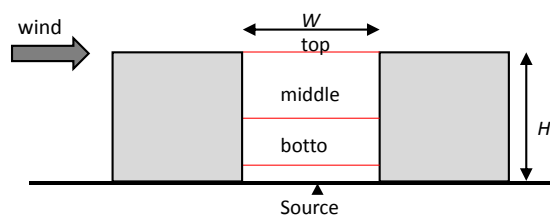
675

676

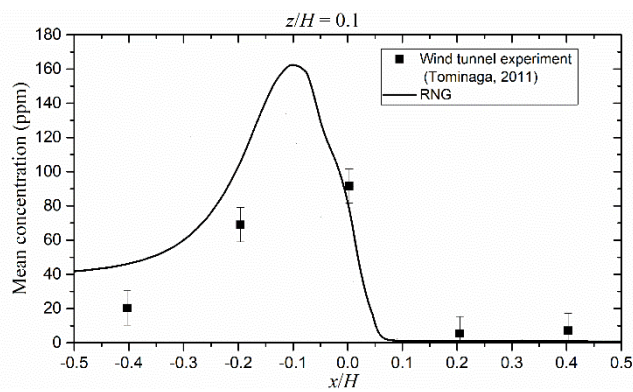


677

678

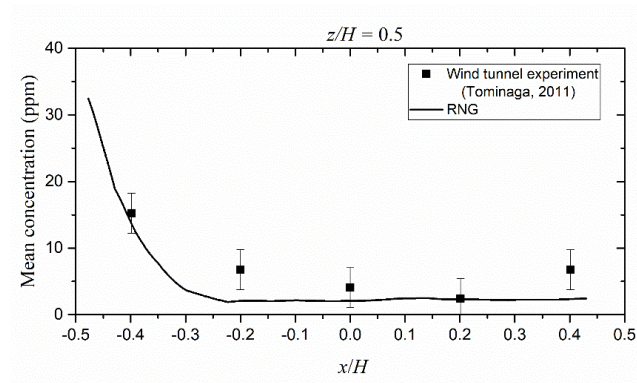


(c)

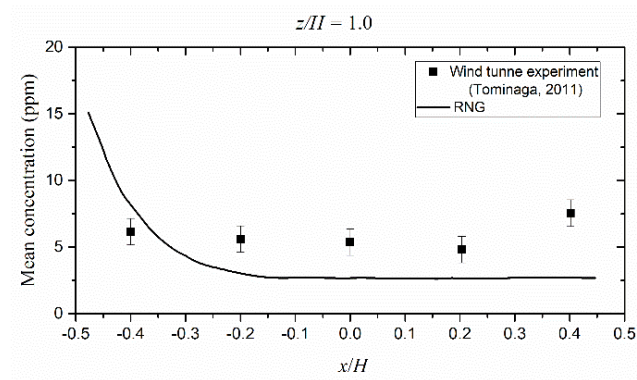


(d) Bottom line ($z/H = 0.1$)

681
682



(e) Middle line ($z/H = 0.5$)

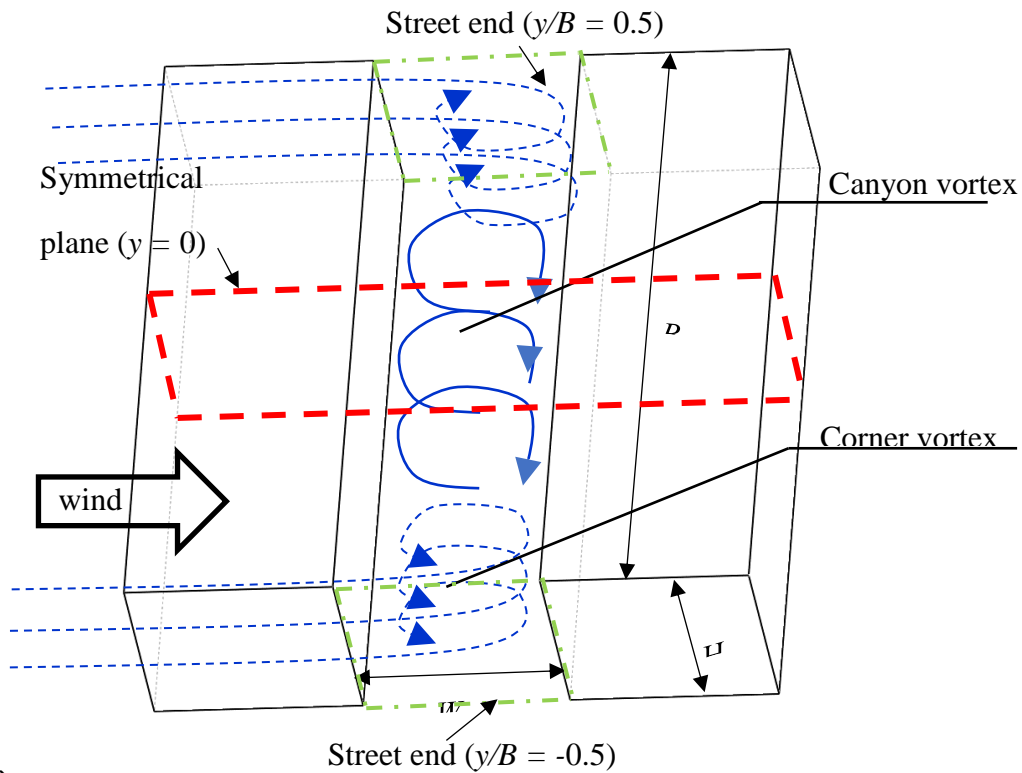


(f) top line ($z/H = 1.0$)

683
684
685
686
687
688
689

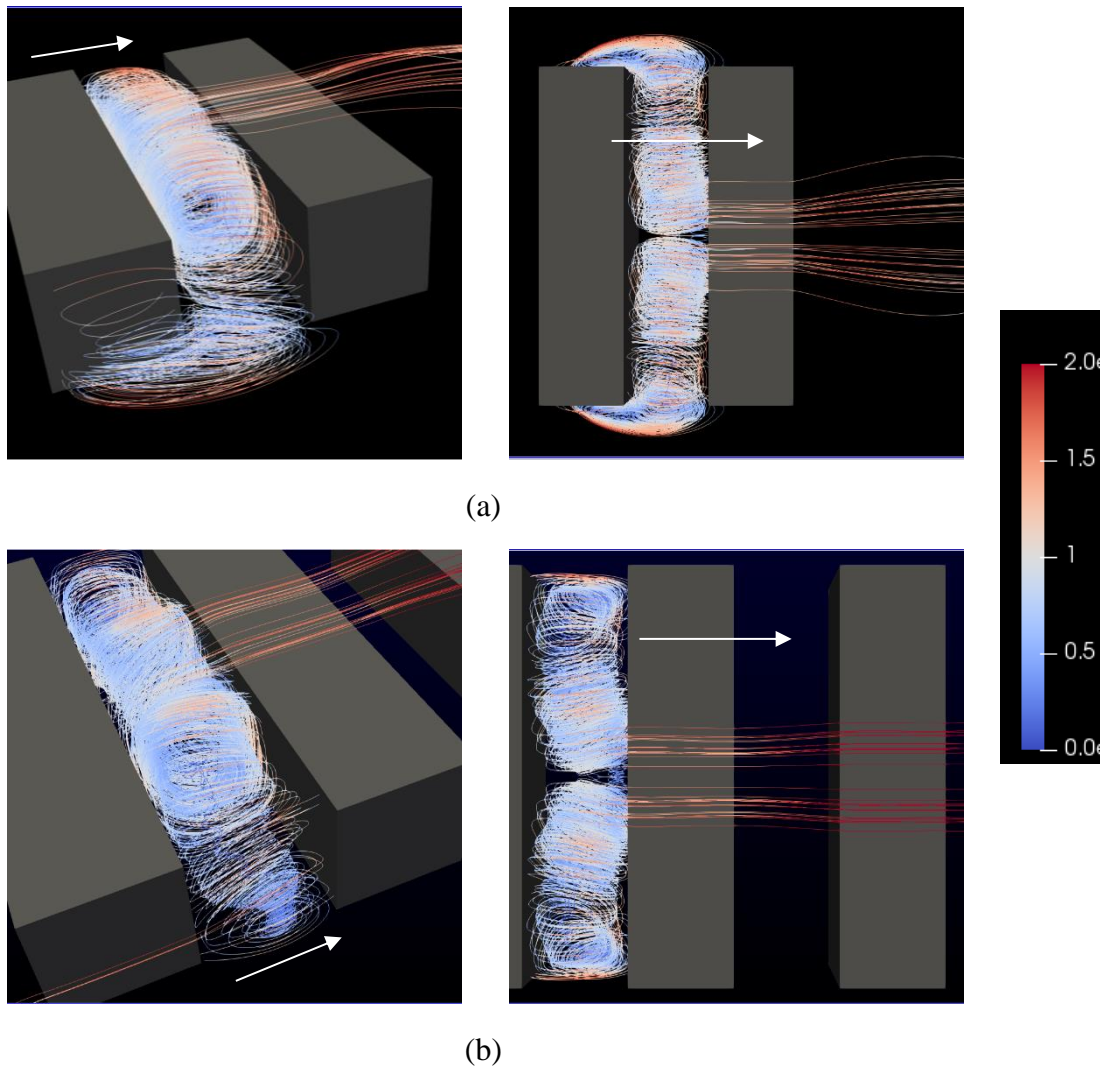
Fig. 4. Comparison of time-averaged concentration c inside a street canyon at three different heights of the symmetrical plane between the present RNG $k-\epsilon$ simulation and previous wind tunnel experiment.

690 Figure 5
691
692
693
694
695
696



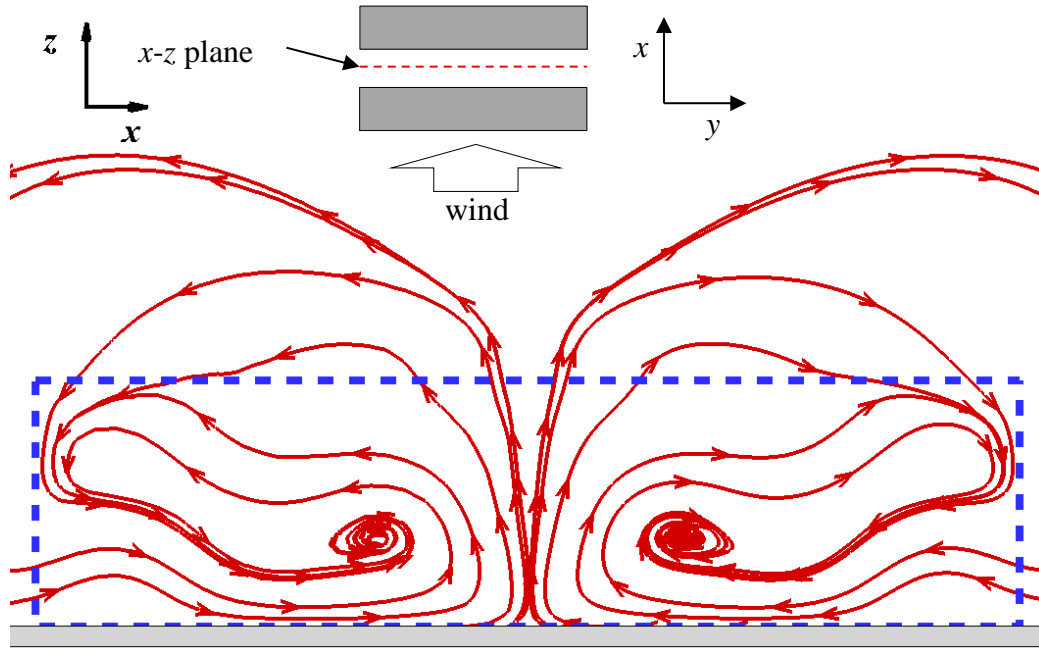
697
698 **Fig. 5.** Schematic illustration of the flow pattern within a 3-D street canyon surrounded
699 by urban buildings and subjected to perpendicular approaching wind. The location of
700 street ends and symmetrical planes are presented. The wind blows from the left to the
701 right.
702
703
704
705
706
707
708
709
710
711

712 Figure 6
713
714
715
716
717
718
719
720
721



722 **Fig. 6.** 3-D streamline in street canyons with ($H/W = 1.0$, $B/W = 4.0$) for isolated street
723 canyon (a) and multiple canyons (b). The streamlines are coloured by mean velocity.
724 Streamlines are originated from multiple seed locations on a straight line above the line
725 source ($z/H = 0.1$). The ambient wind blows from the left to the right.
726
727

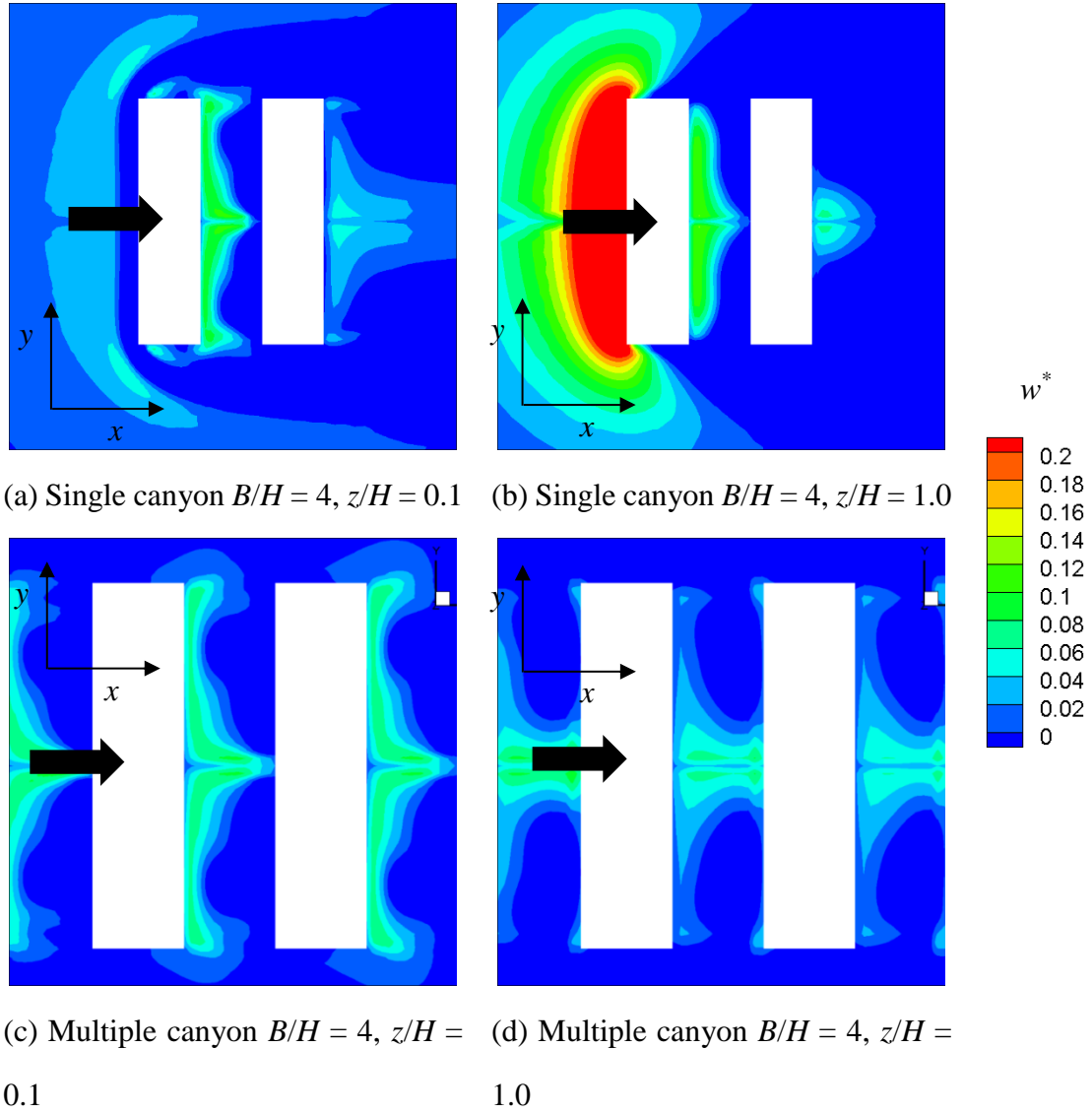
728 Figure 7
729
730
731
732
733
734
735



736
737 Fig. 7. Filtered streamlines plotted at the vertical plane (x - z plane, located at the street
738 centreline, shown as red dash) for cases with $H/W = 1$ and $B/W = 4$. Noted that the x -
739 velocity was filtered as zero at that plane to transfer 3D streamlines into 2D streamlines.

740
741
742
743
744
745
746
747
748
749
750
751
752
753 Figure 8

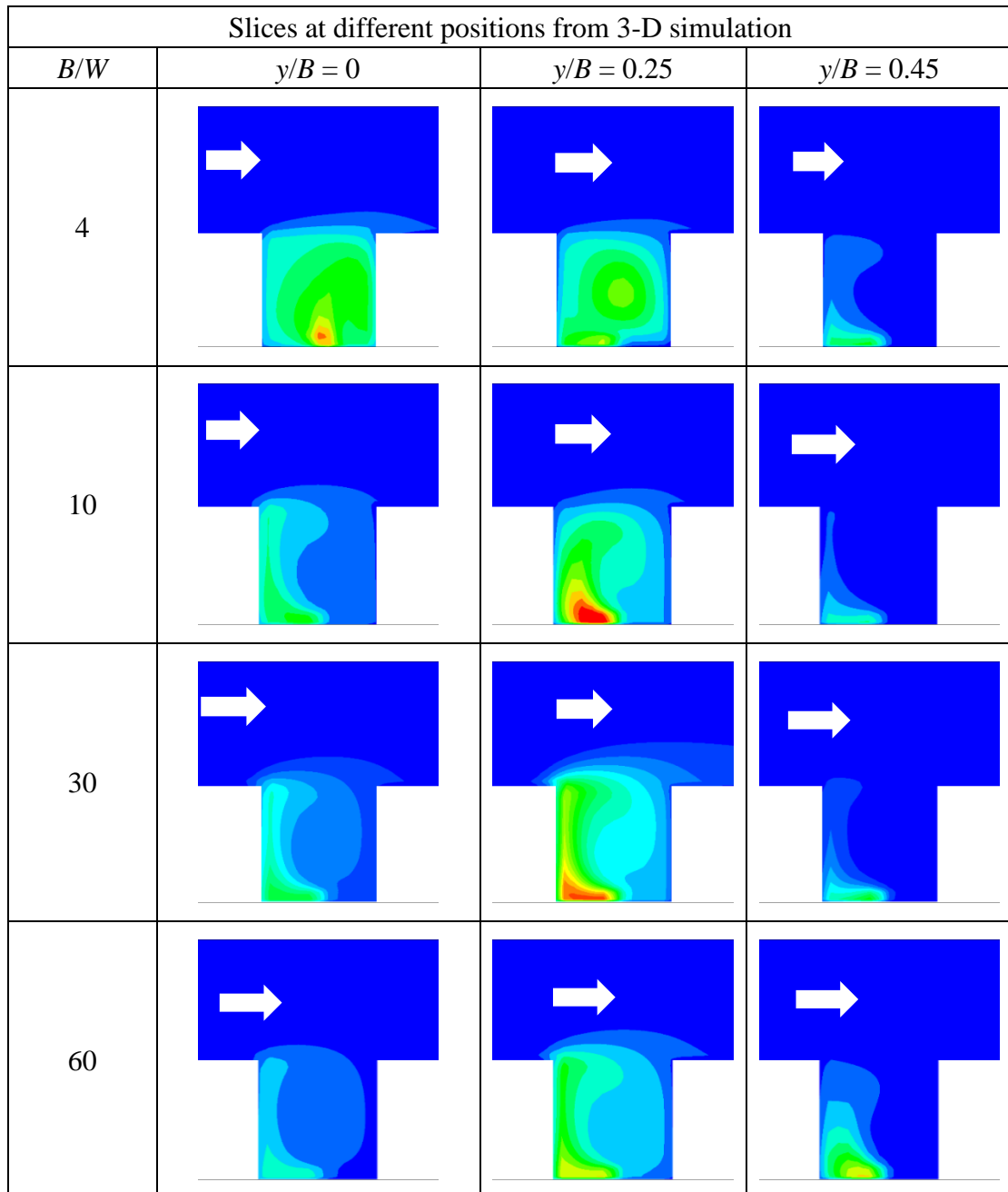
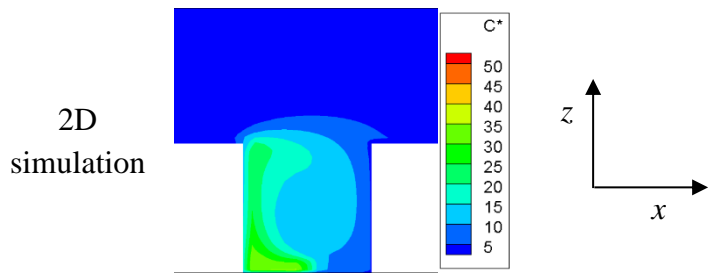
754
755
756
757



758
759
760
761
762
763
764
765
766
767

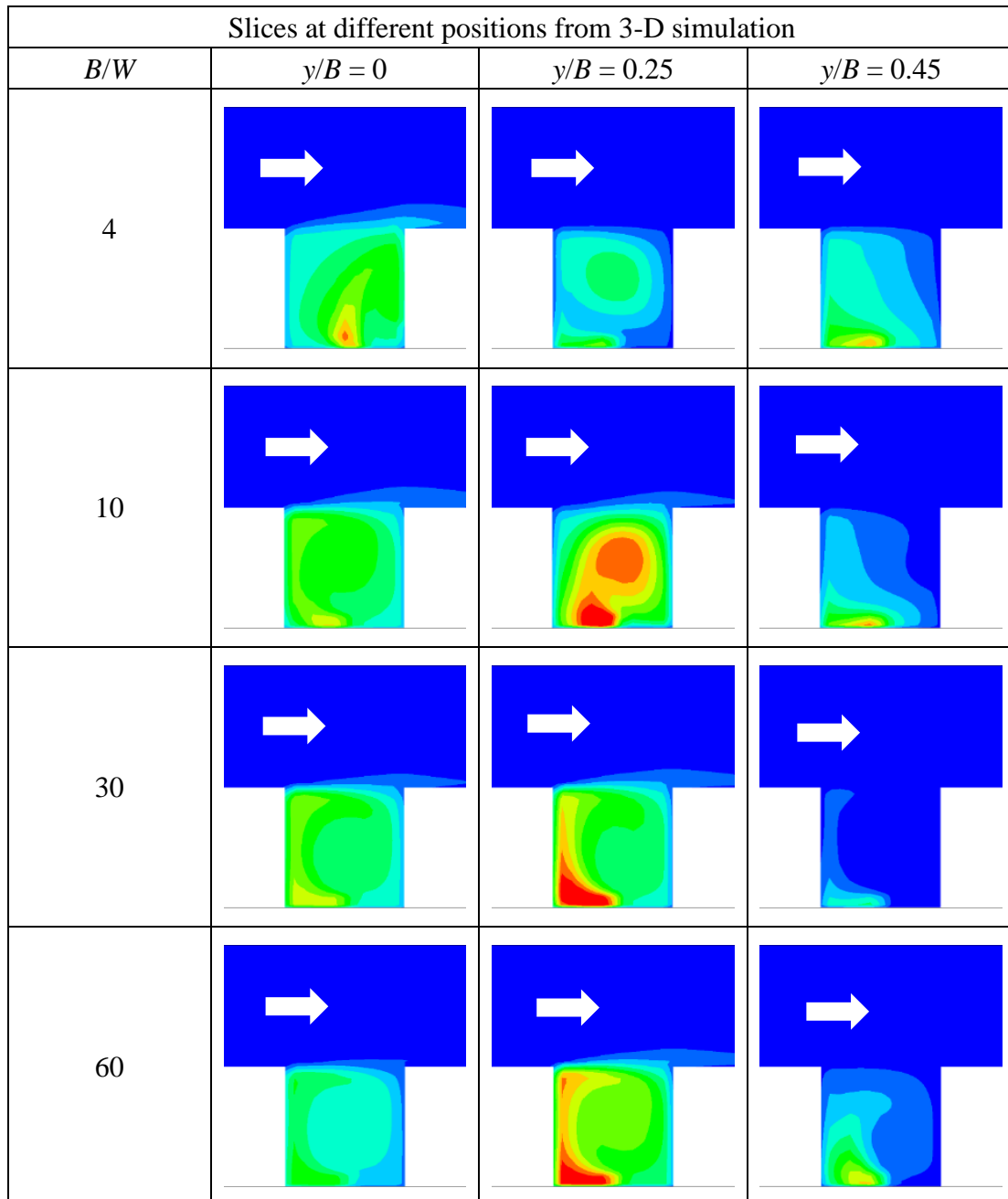
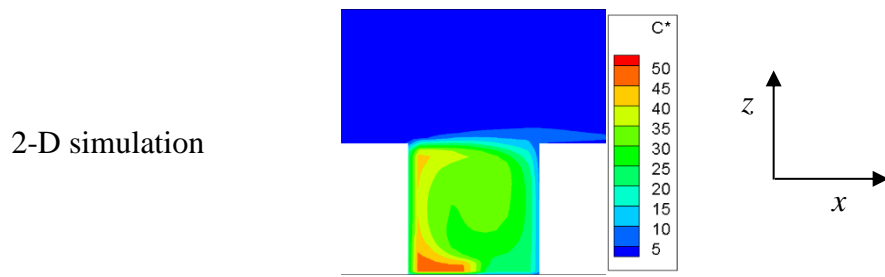
Fig. 8. The normalized mean vertical velocity $w^* = w/U_{\text{ref}}$ at two different height of $z = 0.1H$ and $1.0H$ for cases with $H/W = 1$ and $B/W = 4$. The ambient wind blows from the left to the right.

Figure 9



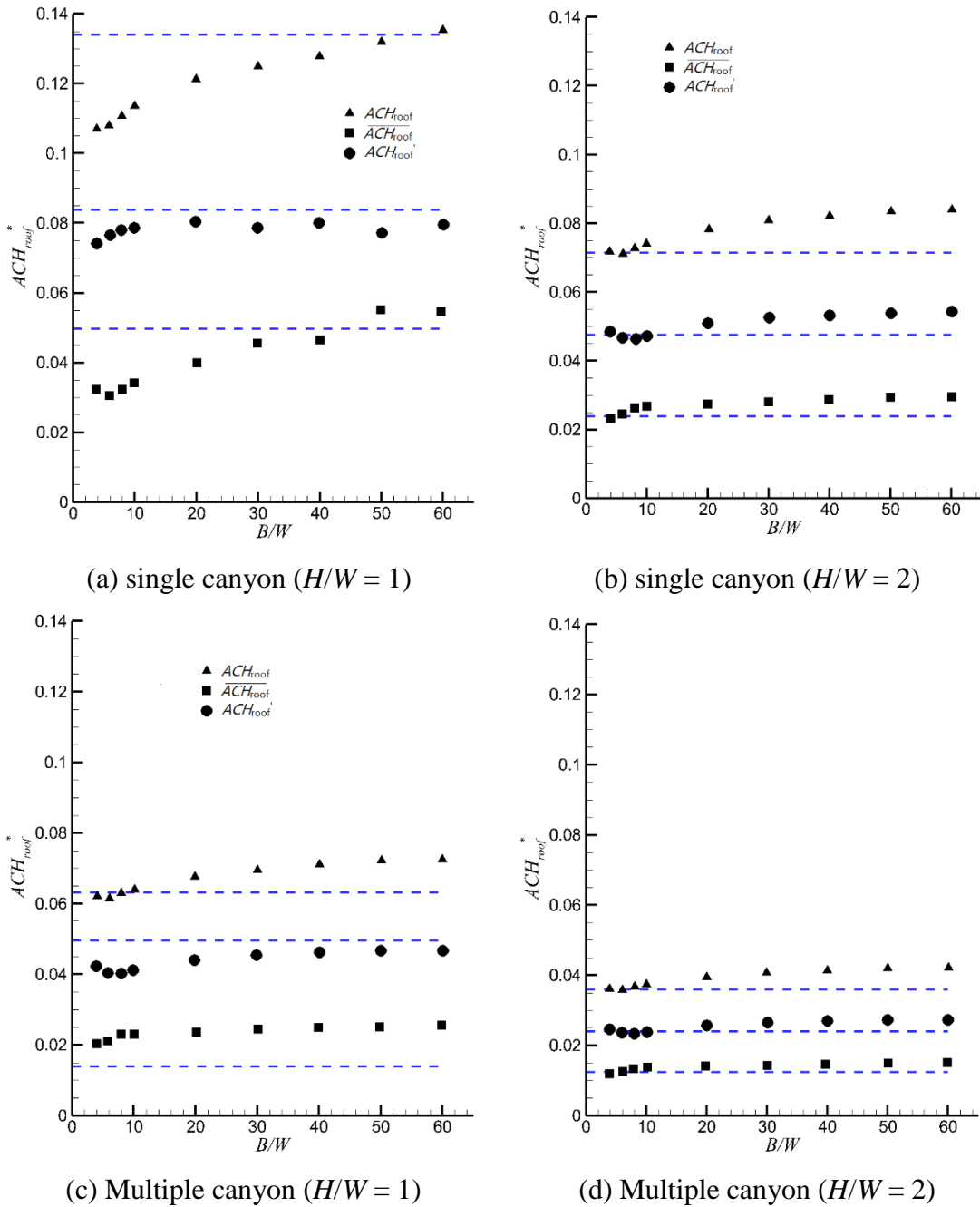
768 **Fig. 9.** Normalized pollutant concentration at 2-D simulation and y -planes for 3-D street
 769 canyon with isolated canyon and $H/W = 1.0$. The ambient wind blows from the left to the
 770 right.

771 Figure 10



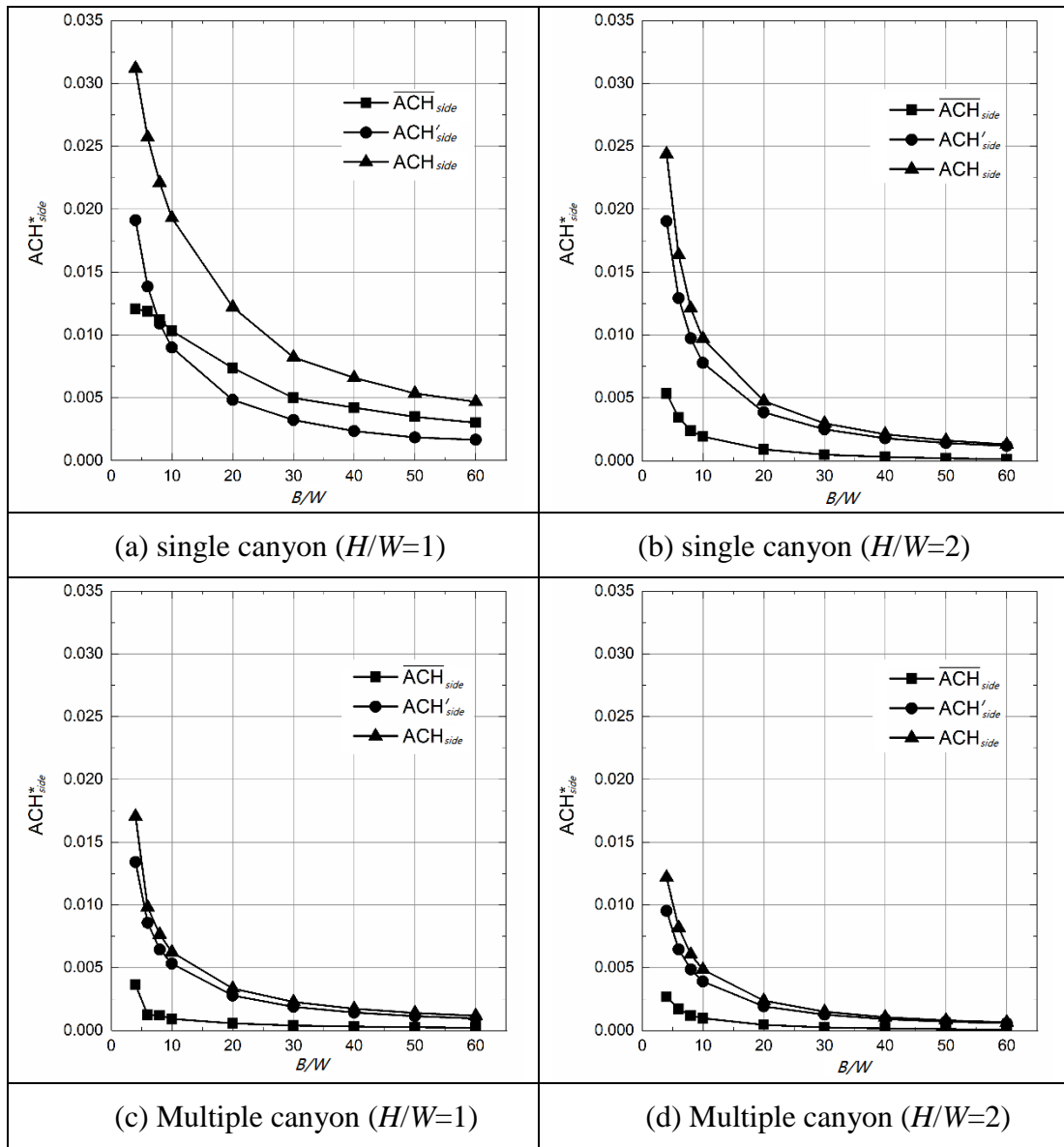
772 **Fig. 10.** Normalized pollutant concentration at 2-D simulation and y-planes for 3-D street
 773 canyon with multiple canyon and $H/W = 1.0$. The ambient wind blows from the left to the
 774 right.

775 Figure 11



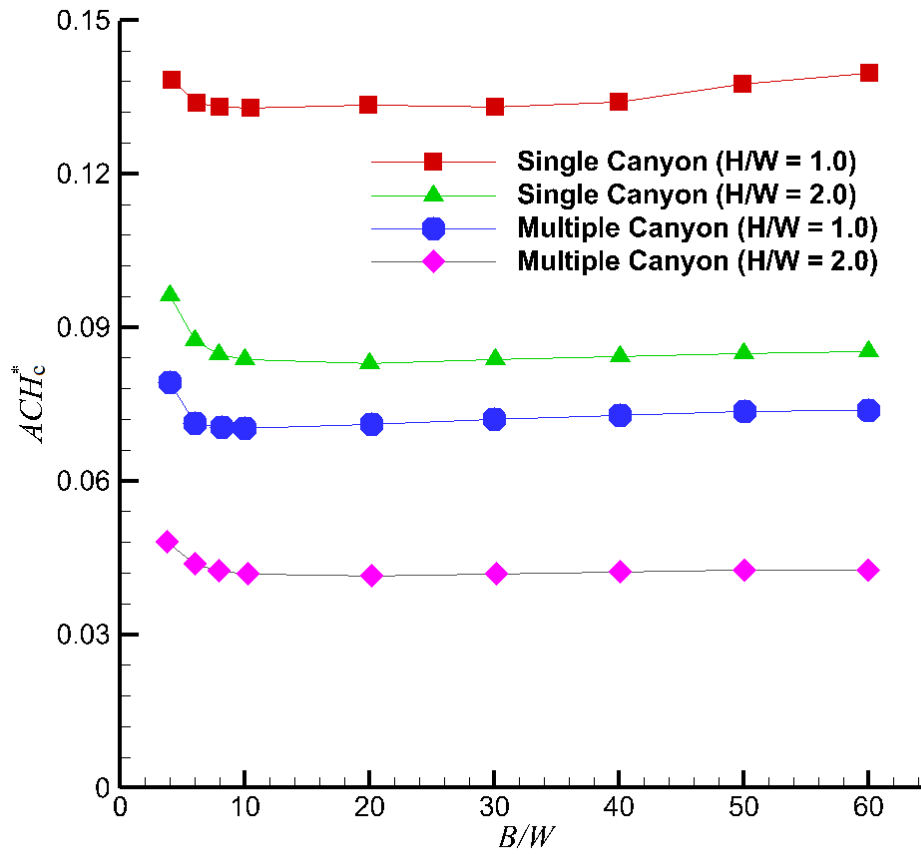
777 **Fig. 11.** Relationship between street length (B/W) and the overall air exchange rate (
 778 ACH_{roof}), mean exchange rate ($\overline{ACH_{roof}}$) and turbulent exchange rate (ACH'_{roof}) at the roof.
 779 The air exchange rates are normalized as ACH^* ($= ACH/U_{ref}$). The results of 2-D
 780 simulation are plotted as blue dash lines.
 781 Figure 12

782
783
784



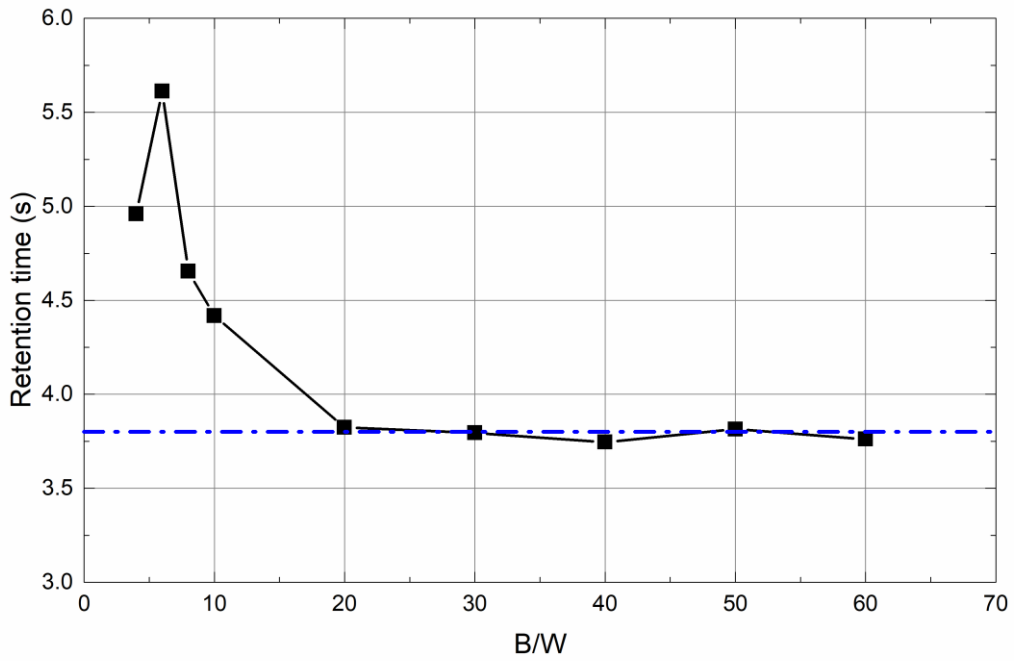
785 **Fig. 12.** Relationship between street length (B/W) and the overall air exchange rate (
786 ACH_{side}), mean exchange rate (\overline{ACH}_{side}) and turbulent exchange rate (ACH'_{side}) at the street
787 ends. The air exchange rates are normalized as ACH^* ($= ACH/U_{ref}$). The results of 2-D
788 simulation are plotted as blue dash lines.
789
790
791

792 Figure 13
793
794
795
796
797
798



799
800 **Fig. 13.** The overall air exchange rate (ACH_c^*) of the whole street canyon against B/W (B
801 the street length, W the street width).
802
803
804
805
806
807
808
809
810
811

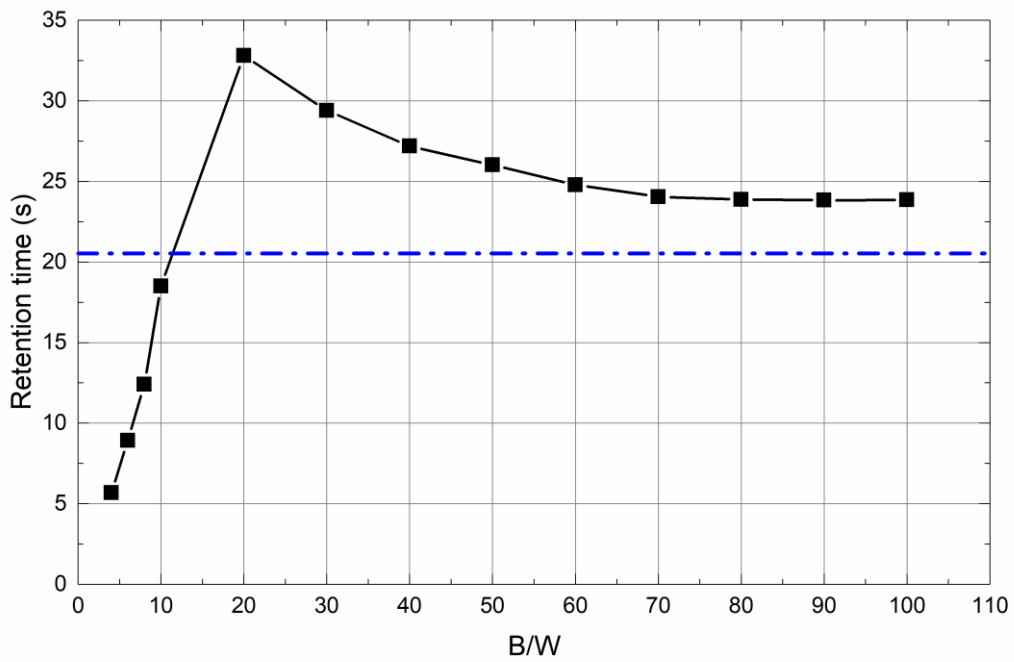
812 Figure 14



813

814

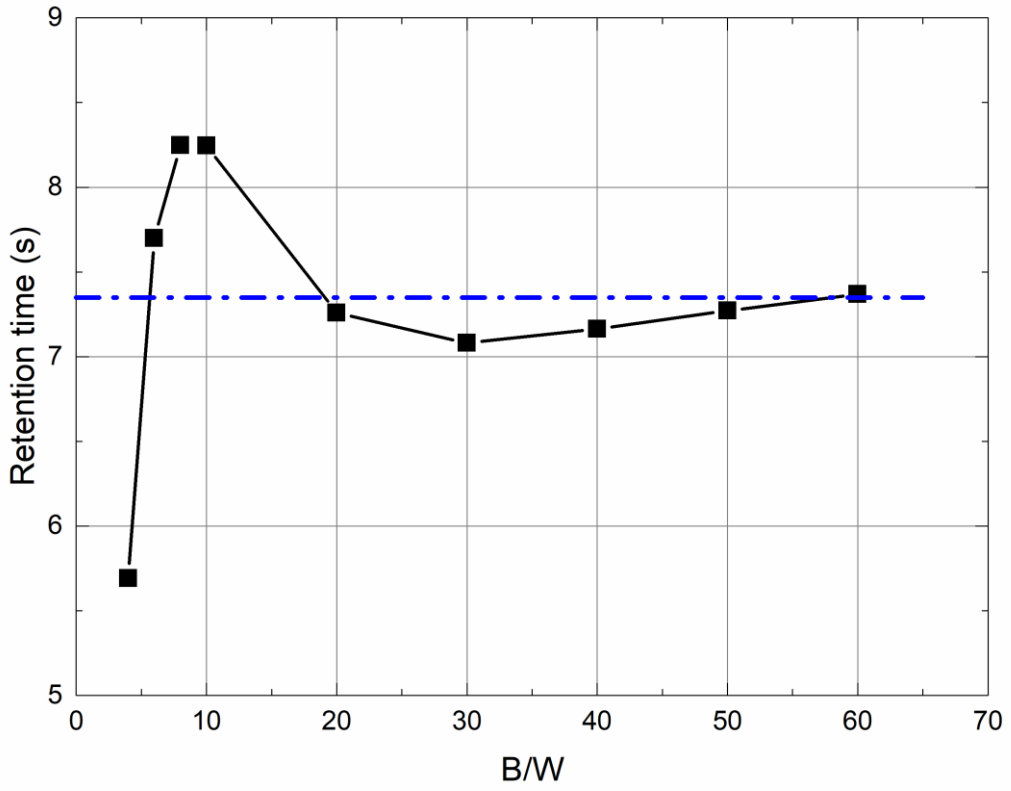
(a) Isolated canyon ($H/W = 1.0$)



815

816

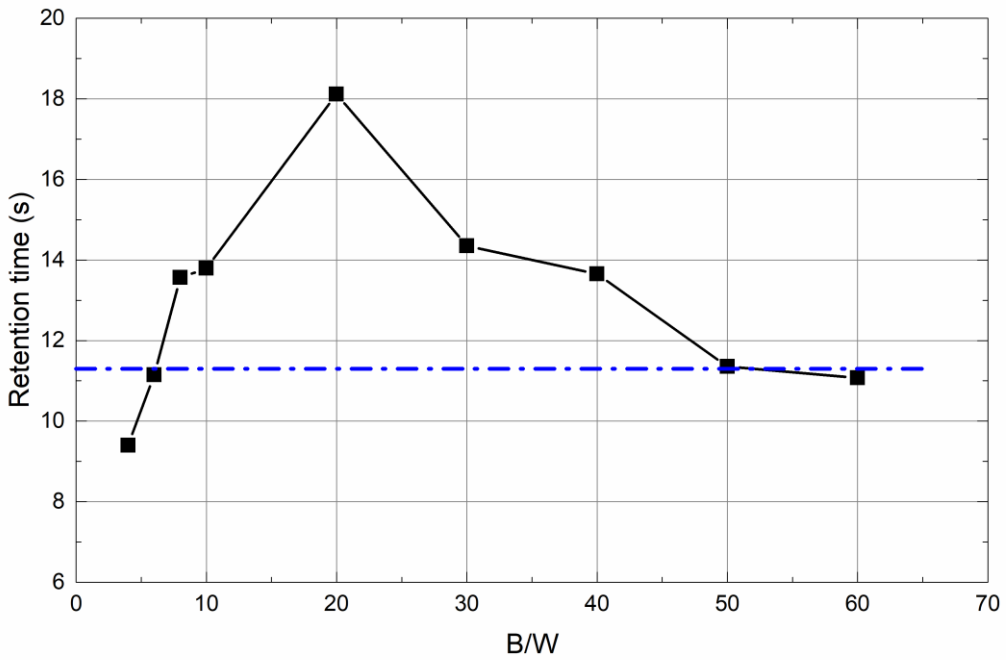
(b) Isolated canyon ($H/W = 2.0$)



817

818

(c) Multiple canyon ($H/W = 1.0$)



819

820

821

822

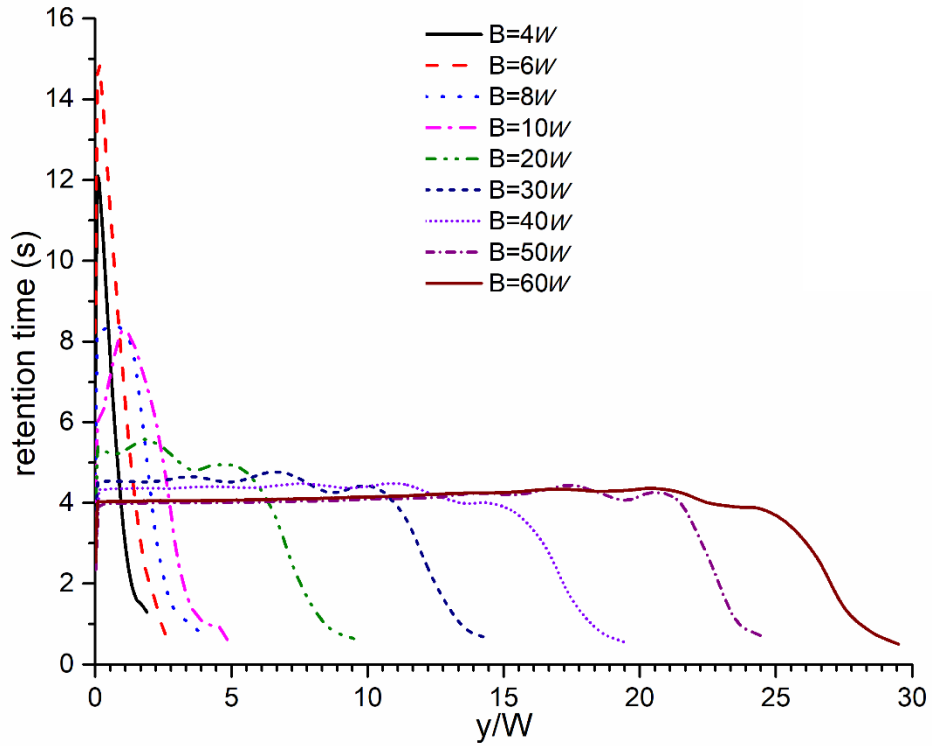
(d) Multiple canyon ($H/W = 2.0$)

Fig. 14. Canyon retention time τ_c against street length B/W .

823 Figure 15

824

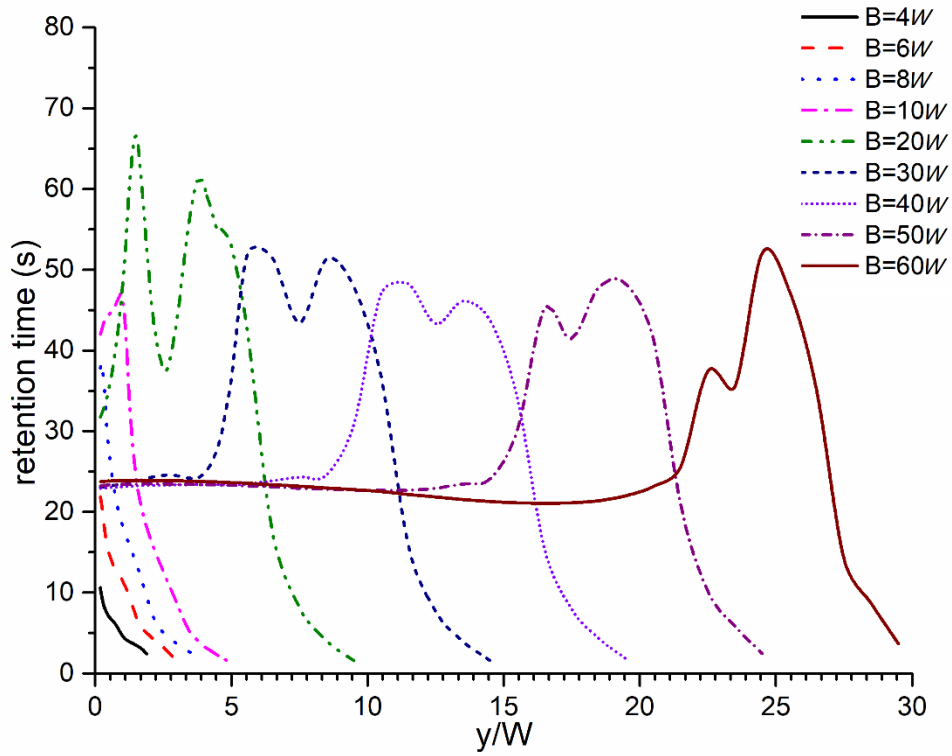
825



826

827

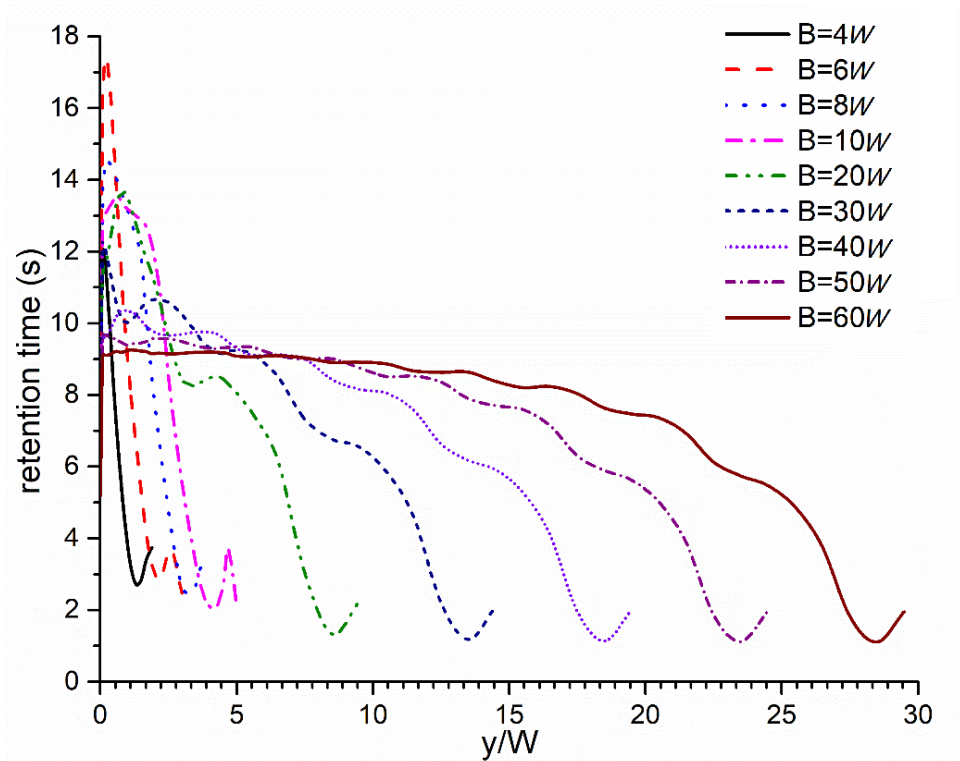
(a) Isolated canyon ($H/W = 1.0$)



828

829

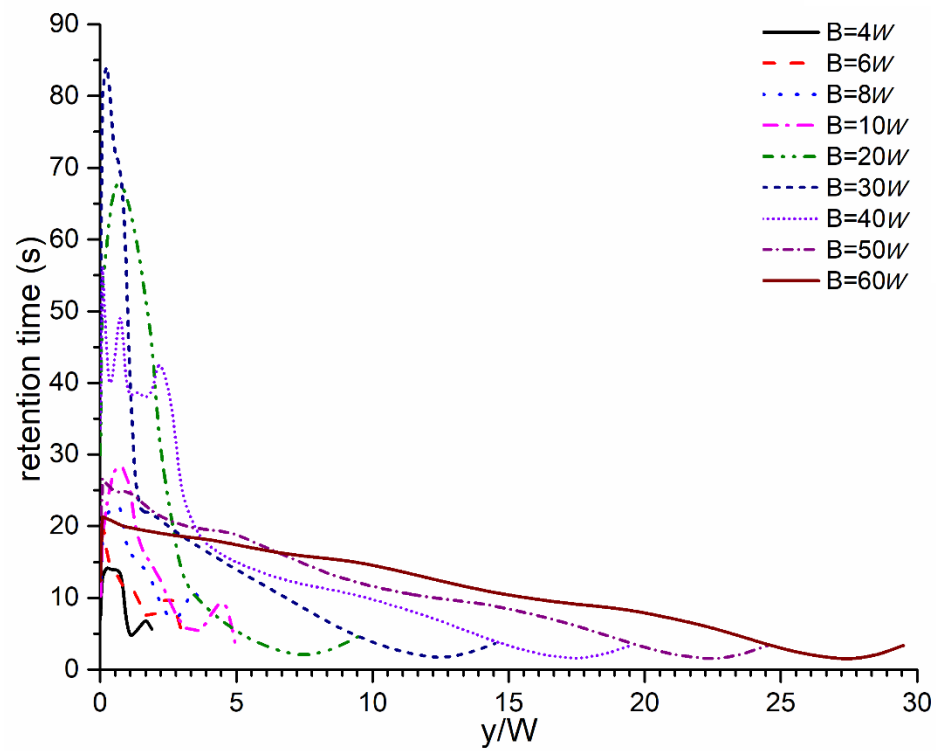
(b) Isolated canyon ($H/W = 2.0$)



830

831

(c) Multiple canyon ($H/W = 1.0$)



832

833

834

(d) Multiple canyon ($H/W = 2.0$)

Fig. 15. Distribution of averaged retention time along street direction (y-direction).